Tectonics

RESEARCH ARTICLE
10.1029/2022TC007248

Dating Low-Grade Deformation: Role of Lithology and Strain Partitioning on Ar Isotope Records in the Alpi Apuane of Northern Apennines (Italy)

Gianfranco Di Vincenzo[1], Gaston Godard[2], and Giancarlo Molli[3]

[1]Istituto di Geoscienze e Georisorse, Consiglio Nazionale delle Ricerche, Pisa, Italy, [2]Université Paris Cité, Institut de Physique du Globe de Paris, UMR CNRS 7154, Paris, France, [3]Dipartimento Scienze della Terra, Università di Pisa, Pisa, Italy

Key Points:

- Intrasample scatter of ^{40}Ar-^{39}Ar in situ ages is due to partial reequilibration of white mica along a deformation path lasting at least 10 Ma
- Chemical and isotope reequilibration of white mica was more pronounced in pelitic layers because of compositionally driven strain partitioning
- Onset of deformation in the Alpi Apuane has a minimum age of ~20 Ma and D2 deformation started not after ~12.5 Ma and ended at ~10.5 Ma

Supporting Information:

Supporting Information may be found in the online version of this article.

Correspondence to:

G. Di Vincenzo,
gianfranco.divincenzo@igg.cnr.it

Citation:

Di Vincenzo, G., Godard, G., & Molli, G. (2022). Dating low-grade deformation: Role of lithology and strain partitioning on Ar isotope records in the Alpi Apuane of northern Apennines (Italy). *Tectonics*, *41*, e2022TC007248. https://doi.org/10.1029/2022TC007248

Received 4 FEB 2022
Accepted 16 JUN 2022

Author Contributions:

Conceptualization: Gianfranco Di Vincenzo, Gaston Godard, Giancarlo Molli
Formal analysis: Gianfranco Di Vincenzo, Gaston Godard
Funding acquisition: Gianfranco Di Vincenzo, Giancarlo Molli
Methodology: Gianfranco Di Vincenzo, Gaston Godard
Project Administration: Gianfranco Di Vincenzo

Abstract The Alpi Apuane (northern Apennines) represent a key area for understanding the processes related to the Apennines building and geodynamic evolution of the central Mediterranean, but the timing of tectono-metamorphic events is still debated. White mica from cover rocks of the Massa and Apuane units was investigated by the ^{40}Ar-^{39}Ar in situ and step-heating techniques. Samples recorded several episodes of deformation developed under low-grade conditions and resulting in a D1 composite schistosity followed by a variably developed D2 retrograde crenulation. In the Massa Unit, D2 crenulation was accompanied by replacement of muscovite-phengite by paragonite, whereas the composition of phengite from the Apuane Unit does not vary noticeably, irrespective of whether phengite is aligned along D1 or D2 schistosities. Both units exhibit a significant intrasample scatter of in situ ages and variably discordant age spectra from step-heating data, due to partial reequilibration of white mica along a deformation path lasting ≥10 Ma, with dates approaching the time of younger events as retrogression becomes more pervasive. The onset of deformation has a minimum age of ~20 Ma, as documented by ^{40}Ar-^{39}Ar data for the composite D1 foliation in the Massa Unit. D2 deformation shows a common temporal evolution at the scale of the region and is recorded for at least ~2.5 Ma, starting not after ~12.5 Ma and ending at ~10.5 Ma. Results highlight the importance of a detailed microscale characterization and of a careful preselection of samples, as compositionally different domains a few millimeters apart may yield different results because of compositionally driven strain partitioning.

1. Introduction

Unraveling the timescale of deformation is one of the key topics in understanding mountain building processes. Chronological data may provide estimates of the age, duration, and rate of deformation events, thus enabling comparison with theoretical modeling. For these purposes, white micas are ideal minerals to be investigated. They are among the most common minerals in metamorphic rocks, can (re)crystallize in response to deformation events, and their fabrics provide an important means to establish the temporal relationship between tectonic activity and growth of the index minerals. White micas exhibit a number of chemical substitutions (e.g., Guidotti, 1984), which make them stable under different *P-T* regimes. Additionally, the high potassium content of potassic white micas allows analyses on comparatively smaller samples through the ^{40}Ar-^{39}Ar method, facilitating the application of laser extraction techniques for in situ dating at high spatial resolution. The potential of white micas in deformation studies has even recently increased due to improved precision of ^{40}Ar-^{39}Ar data, thanks to a new generation of multicollector noble gas mass spectrometers (e.g., Jicha et al., 2016; Mark et al., 2009; Mixon et al., 2022; Phillips & Matchan, 2013) together with efforts to improve accuracy by calibration of mineral standards through astronomical tuning (see e.g., Kuiper et al., 2008; Niespolo et al., 2017).

The argon-retentive properties of white mica are still rather debated. The most recent experimental work (Harrison et al., 2009) has yielded diffusion parameters that give theoretical closure temperatures slightly higher than previously thought (~350°C – McDougall & Harrison, 1999), ranging from ~400 to 460°C for white micas with diffusive radii of 100–500 μm and which cool down at 10°C/Ma under a pressure of 0.5 GPa. More recently, Nteme et al. (2022) using atomistic simulations have obtained theoretical diffusion parameters that yield closure temperatures (for cooling rates ranging from 1 to 100°C/Ma and grain sizes from 0.1 to 1.0 mm) close to the upper stability limit of muscovite (in the range of 560–800°C). Some authors have questioned the reliability of laboratory diffusion experiments for hydrous mineral phases because of crystallographic changes during in vacuo

Validation: Gianfranco Di Vincenzo, Gaston Godard, Giancarlo Molli
Writing – original draft: Gianfranco Di Vincenzo
Writing – review & editing: Gianfranco Di Vincenzo, Gaston Godard, Giancarlo Molli

heating and/or the presence of mineral impurities (Villa, 2021; Villa & Hanchar, 2017; Villa & Puxeddu, 1994). These drawbacks inevitably lead to an underestimation of the true retentive properties of the pure and mineralogically stable mineral. Consistent with this view, several field-based studies have shown that white mica that escaped successive recrystallization can preserve Ar isotope records of earlier metamorphic events even if reheated under temperature conditions up to 500–550°C (e.g., Augier et al., 2005; Di Vincenzo et al., 2004; Villa et al., 2014), in agreement with the observation that the intergranular cation diffusion in white micas is insignificant below ~550°C (Dempster, 1992). Recent research has also shown that reequilibration of white mica in low-to medium-grade metamorphic rocks, in response to superimposed tectono-metamorphic events, occurs through dissolution-reprecipitation reactions, which typically result in complex submillimeter textural/chemical heterogeneities due to incomplete equilibrium (Airaghi, Lanari, et al., 2017; Airaghi, Warren, et al., 2017; Akker et al., 2021; Beaudoin et al., 2020; McAleer et al., 2021). Dating deformation in low-grade metamorphic rocks may therefore be particularly challenging due to the surviving of mineral and/or compositional relicts, including a detrital component, and to the potential high partitioning of superimposed deformation events between quartzo-feldspathic and phyllosilicate-rich domains (e.g., Airaghi, Lanari, et al., 2017; Akker et al., 2021; Beaudoin et al., 2020; Cardello et al., 2019; Di Vincenzo et al., 2016, 2004).

The Alpi Apuane region, with exposure of synorogenically exhumed low-grade metamorphic rocks, represents a key area for understanding the processes related to the Apennines building and the geodynamic evolution of the central Mediterranean area (Carmignani et al., 1978; Carmignani & Kligfield, 1990; Jolivet et al., 1998; Le Breton et al., 2017). Geochronological studies in the region dated back to the early 70s (Giglia & Radicati di Brozolo, 1970) and were refined during the 1980s, with a first attempt to date superimposed structures and fabrics related to the progressive deformation history that affected the region during the Tertiary (Kligfield et al., 1986). While the most recent contributions focused on timing of the late- and postmetamorphic tectonic evolution by low-temperature thermochronology (Abbate et al., 1994; Fellin et al., 2007), some problems related to the timing of the early tectonic history were raised (Costa et al., 1998; Patacca et al., 2013). More specifically, Patacca et al. (2013), on the basis of an interpretation of the micropaleontological and geological records of the turbiditic metasandstones of the Pseudomacigno Formation (the youngest rock type of the Alpi Apuane metasedimentary sequence), questioned the meaning of the oldest (~27 Ma) ages reported by Kligfield et al. (1986) and considered the onset of the D1 deformation at the Rupelian/Chattian boundary geologically unrealistic. According to these authors, ages not older than ~13–14 Ma would be expected for the metamorphism in the Alpi Apuane. The fact that the geochronological data are older than 30 years and the timing of tectono-metamorphic events in the Alpi Apuane represents a first order constraint for kinematic interpretation of the Apennines further led us to see the Alpi Apuane as an ideal case study for investigating the issues involved in ^{40}Ar-^{39}Ar dating deformation of low-grade metamorphic rocks.

In this work, we take advantage of the analytical performance of the ARGUS VI multicollector noble gas mass spectrometer in unraveling the deformation history of metasedimentary units of the Alpi Apuane (northern Apennine), which were involved in the Adria continental margin subduction and syn- to post-contractional exhumation. ^{40}Ar-^{39}Ar in situ data on rock chips, supplemented by a detailed structural, textural, and chemical characterization down to the microscale, are compared with step-heating data from bulk mineral separates, which were completed through an old generation single-collector noble gas mass spectrometer. Results reveal a complex picture that highlights the role of lithology and strain partitioning on the Ar isotope record of low-grade metamorphic rocks and, from a broad perspective, reiterates the importance of microscale textural and chemical characterization for a correct interpretation of ^{40}Ar-^{39}Ar data.

2. Geological Background and Rationale

2.1. Geological Framework

The Alpi Apuane represents the largest tectonic window in the inner northern Apennines, a Cenozoic stack of oceanic Ligurian Tethys-derived units overthrusted with an eastward vergence on top of continental Adria-derived tectonic units. These latter, exposed in and around the Alpi Apuane, represent the originally distal Adria continental margin of the so-called Tuscan domain, whereas the proximal margin is witnessed in the external zone of the Umbria-Marche fold and thrust belt (Figure 1). Three major stratigraphic and tectono-metamorphic continental-derived units are traditionally distinguished in the Alpi Apuane: (a) the Tuscan Nappe, (b) the Apuane Unit, and (c) the Massa Unit, the latter two collectively known as Tuscan metamorphic units (Figure 1).

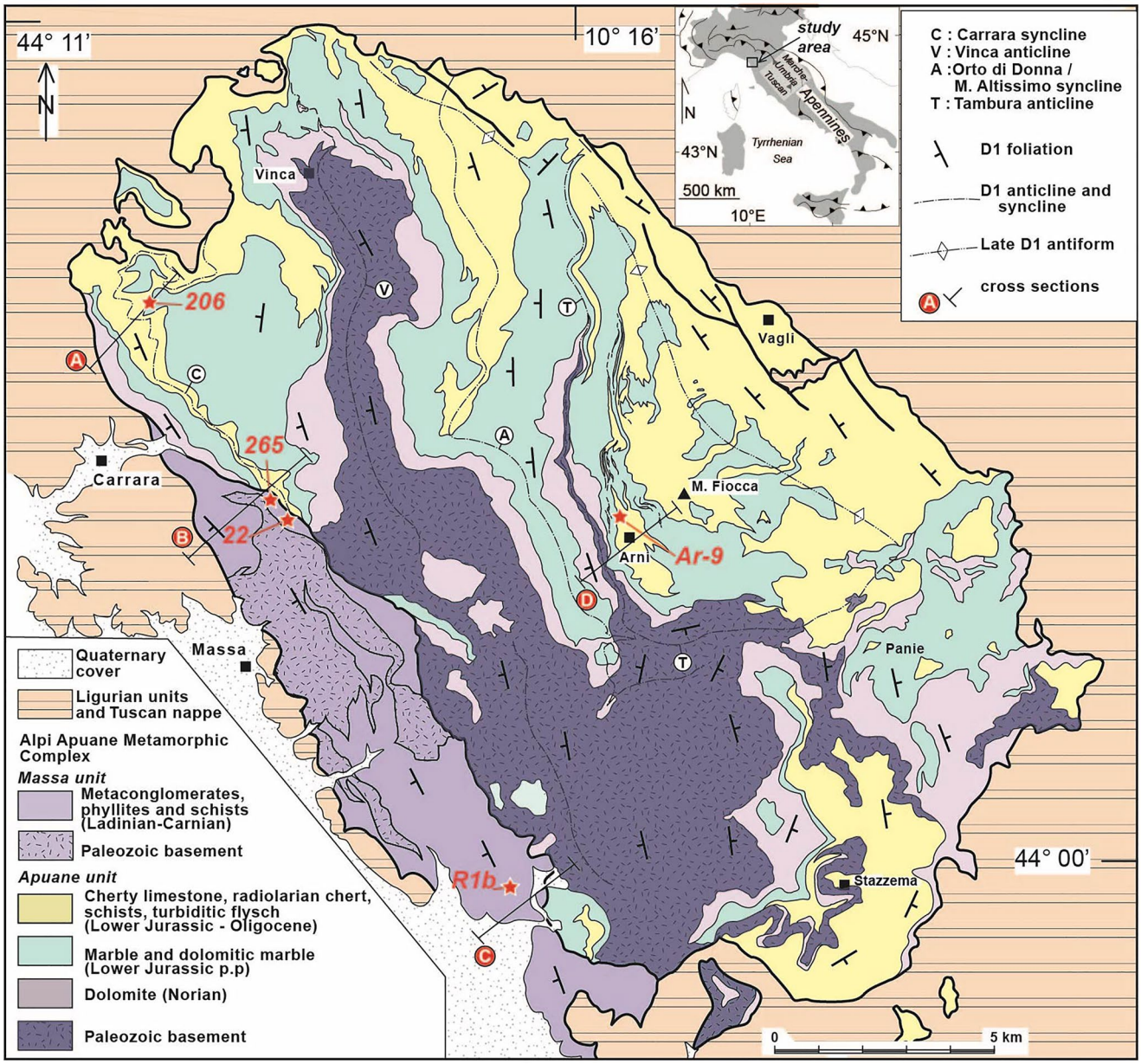

Figure 1. Simplified geological map of the Alpi Apuane with sample locations (modified after Molli et al., 2018).

The Tuscan Nappe consists of Mesozoic carbonate rocks and Tertiary deep water and turbiditic sequences mainly detached from their original basement along the décollement level of the former Carnian and Norian anhydrites and dolostones (Ciarapica & Passeri, 2002). The protolith was almost everywhere transformed during the orogenic deformation into cataclastic carbonate-rich breccia, known as *Calcare Cavernoso* (Conti et al., 2020). The post-Norian sequence continues with Rhaetian to Hettangian shallow water limestones (Rhaetavicula Contorta and Calcare Massiccio), Lower Jurassic to Cretaceous pelagic limestones, radiolarites and shales (i.e., Calcare Selcifero, Marne a Posidonomya, Diaspri, and Maiolica), grading to hemipelagic deposits of the Scaglia (Cretaceous-Oligocene), to end with the siliciclastic foredeep turbidites of the Macigno (late Oligocene-early Miocene, Conti et al., 2020).

The Apuane Unit forms most of the Alpi Apuane tectonic window and is made up of a Paleozoic basement unconformably overlain by an Upper Triassic-Oligocene metasedimentary sequence. The Paleozoic basement consists of metasedimentary and metavolcanic rocks, including Cambrian-Lower Ordovician phyllites and

quartzites, Middle Ordovician metavolcanics and metavolcanoclastics, Upper Ordovician quarzitic metasandstones and phyllites, Silurian black phyllites, and Orthoceras-bearing metadolostones (Conti et al., 1991). These Paleozoic lithostratigraphic units were deformed and metamorphosed under low-grade conditions, during the Variscan orogeny (Conti et al., 1991; Molli et al., 2020) and intruded during early Permian by subvolcanic felsic bodies (Vezzoni et al., 2018). The Mesozoic cover rocks, where the sequence is complete, include thin Triassic continental to shallow-water Verrucano-type deposits followed by Upper Triassic-Lower Jurassic carbonate platform metasediments comprising dolostone (Grezzoni Formation), dolomitic marble, and marble (the Carrara Marble), in turn covered by Lower Jurassic-Lower Cretaceous cherty metalimestone, cherts, and calcschists, and Lower Cretaceous to lower Oligocene sericitic phyllites and calcschists with marble interlayers. Oligocene-early Miocene (?) metasediments related to turbiditic systems (Pseudomacigno Formation) complete the sedimentary succession (Conti et al., 2020).

The Massa Unit is exposed in the westernmost part of the Alpi Apuane tectonic window and includes a litho-stratigraphic sequence formed by a Paleozoic basement similar to that of the Apuane Unit and a characteristic and distinctive Upper Permian-Upper Triassic metasedimentary succession, including a Middle Triassic continental (conglomerates and pelites) to marine (carbonate platform-derived deposits) successions, associated with intraplate alkaline basalts (Martini et al., 1986; Patacca et al., 2011 and reference therein). Lithostratigraphic units younger than the late Middle Triassic are locally found as tectonic lenses and decimeter-scale remnants within a cataclastic fault zone below the contact with the overlaying Tuscan Nappe (Molli et al., 2018).

2.2. Tectono-Metamorphic Evolution

The deformation structures of the Tuscan metamorphic units of the Alpi Apuane were affected by two main tectono-metamorphic regional events (see D1 and D2 phases of Carmignani & Kligfield, 1990), which are regarded (Molli, Conti, et al., 2000, Molli, Giorgetti, & Meccheri, 2000; Molli et al., 2002) as recording progressive deformation of the distal Adriatic continental margin during continental subduction and the syn- to post-collisional exhumation (Carmignani & Kligfield, 1990; Jolivet et al., 1998; Molli, 2008; Molli et al., 2018). The two main regional events, D1 and D2, were related to different fold generations or folding phases (Molli & Meccheri, 2012). The D1 event, which can be associated with underplating and antiformal stacking of the metamorphic units, is defined by a main axial-plane foliation of recumbent isoclinal folds, observable on a millimeter to a kilometer scale (Figure 2) and it is associated with a regionally NE-oriented stretching lineation interpreted as recording the main transport direction of the inner northern Apennines (Carmignani et al., 1978; Molli, 2008). During the D2 event, the D1 structures were reworked by different generations of folds and shear zones, related to postpeak metamorphic exhumation (Molli, 2008). During the early stage of D2, crenulation folds with a characteristic subhorizontal axial plane developed on a regional scale, while successive deformation was associated with semibrittle and brittle structures, represented by kink and open folds, as well as low-angle normal faults (Molli et al., 2018). The final stages of deformation and erosion-driven unroofing and exhumation are recorded by systems of high-angle normal to oblique-normal and transcurrent faults, related with the recent to active deformation regime affecting the area (Molli et al., 2021).

In the Tuscan metamorphic units of the Alpi Apuane, peak conditions reached ~0.4–1.0 GPa and ~350–500°C and were attained during the D1 deformation (Figure 3). More specifically, peak conditions for the D1 kyanite + chloritoid + phengitic muscovite assemblage in metapelites of the Massa Unit varied within ~0.6–1.0 GPa and 420–500°C (Franceschelli et al., 1986, 1997; Franceschelli & Memmi, 1999; Jolivet et al., 1998; Molli, Giorgetti, & Meccheri, 2000). Assemblages in D1 fabrics, consisting of pyrophyllite + chloritoid + chlorite + phengitic muscovite in metapelites of the Apuane Unit, gave peak metamorphic estimates in the range of ~0.4–0.6 GPa and ~350–450°C (Franceschelli et al., 1986; Jolivet et al., 1998; Molli, Giorgetti, & Meccheri, 2000).

In contrast to the Tuscan metamorphic units, the Tuscan nappe was accreted at a shallow crustal level within the northern Apennines wedge, from the early Miocene (Cerrina Feroni et al., 1983; Molli, 2008). Burial occurred under a sequence of thrust sheets now preserved in the overlying sub-Ligurian and Ligurian units (Figures 1 and 2). Early thrusting is documented by top-to-the-east decimeter-scale shear zones and an early generation of east-vergent tight to isoclinal folds within incompetent layers, subsequently overprinted by small (decimeter scale) to large (kilometer scale) refolding, and later low-angle normal faults (Carosi et al., 2003; Molli et al., 2011; Storti, 1995). Very low-grade metamorphism, arisen in a temperature range of 250–300°C during burial and deformation, has been documented by Raman spectroscopy on carbonaceous material (RSCM), illite crystallinity

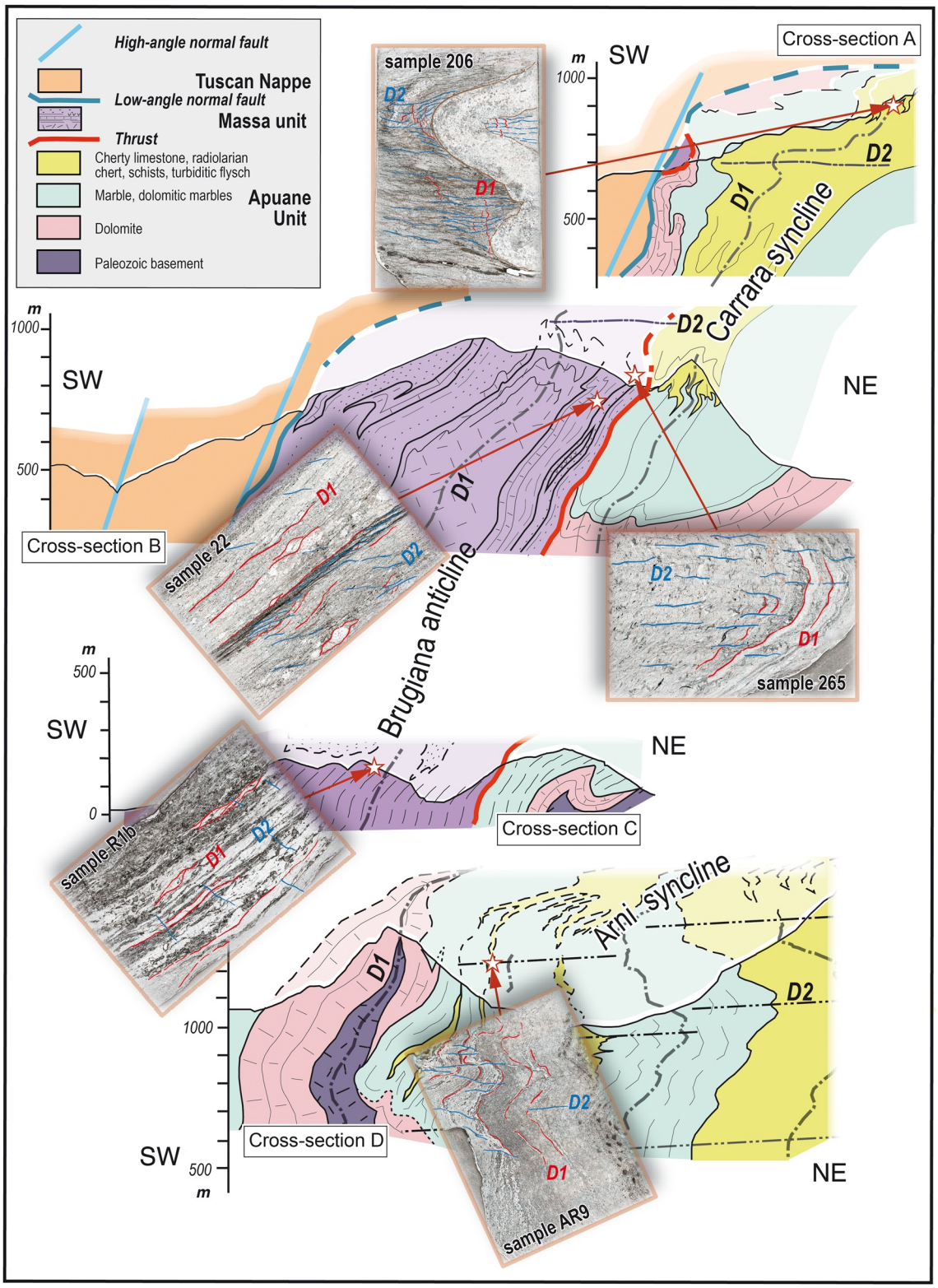

Figure 2. Vertical cross-section with locations of the investigated samples in their own structural setting. The major D1 and D2 structures and their relationships are illustrated together with the original orientation of the studied samples, represented as microphotographs under the optical microscope. Structural relationships at the cartographic to the submillimeter scale are also reported.

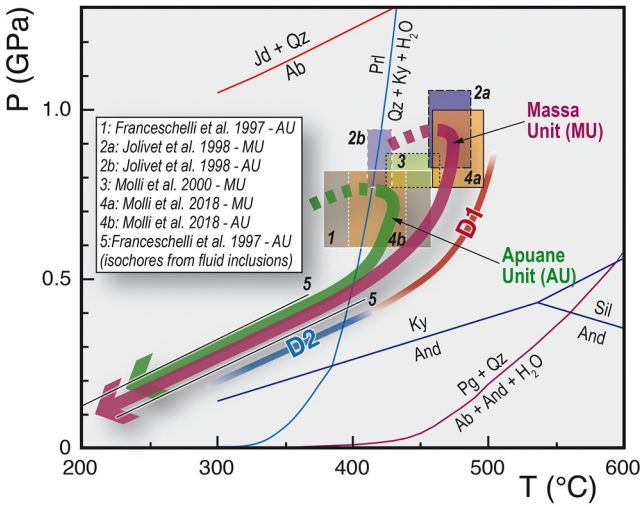

Figure 3. *P-T* estimates and paths for the Apuane and Massa units based on literature data. Data used for boxes 1–3 are derived from quantitative classical thermo-barometry (Franceschelli et al., 1997; Jolivet et al., 1998; Molli, Giorgetti, & Meccheri, 2000). Data used to define box 4 also include temperatures based on Raman spectroscopy on carbonaceous material (RSCM) (Molli et al., 2018). Lines 5 are based on isochores obtained from CO_2 fluid inclusions in barite and fluorite (see Franceschelli et al., 1997). Red and blue lines (D1 and D2) outline the relative timing of deformation D1 and D2 fabrics with changing metamorphic conditions. The univariant curves have been calculated using the software THERMOCALC and an updated version (ds62) of the thermodynamic data set from Holland and Powell (2011).

and fluid inclusion studied and was tectono-stratigraphically constrained to a maximum depth of ~7–10 km (Carosi et al., 2003; Cerrina Feroni et al., 1983; Fellin et al., 2007; Molli et al., 2018).

2.3. Previous Geochronology

Available geochronological data from the Alpi Apuane region are limited to K-Ar data and some conventional ^{40}Ar-^{39}Ar step-heating data, which date back to the early 1970s and the late 1980s. Giglia and Radicati di Brozolo (1970) obtained K-Ar ages on white-mica separates in the range of ~17–11 Ma. Kligfield et al. (1986), using both the K-Ar and ^{40}Ar-^{39}Ar techniques, reported a few tens of K-Ar analyses from fine-grained mica separates and whole rocks from the Apuane Unit, yielding ages ranging from ~27 to ~10 Ma, with age decreasing along with grain size and with the degree of crenulation of the older D1 structures and the progressive development of the D2 structures. These data were used to constrain the major deformation phase D1 to the lower Chattian (~27 Ma), with subsequent increments of deformation ending in the middle Tortonian (~10 Ma). The termination of metamorphism and ductile deformation in the middle Tortonian (~10 Ma) has been confirmed by Fellin et al. (2007), who used low-temperature thermochronology and considered a zircon fission-track closure temperature of ~240°C.

3. Analytical Procedures

Microstructural, microtextural, and microchemical investigations were mainly carried out on polished thin sections derived from the opposite face of rock chips used for ^{40}Ar-^{39}Ar dating. Backscattered electron (BSE) images and X-ray chemical element maps were obtained using a ZEISS Supra 55 VP scanning electron microscope (SEM) at Ecce Terra laboratory (Université Pierre-et-Marie-Curie, Paris, France). Image processing was carried out with Photoshop® (brightness/contrast adjustments and filtering) and ENVI® (principal component analysis and mineral classification). Electron microprobe (EMP) analyses of individual minerals were carried out using a Cameca SX-100 electron microprobe at Camparis laboratory in Paris (Table S1), in the following analytical conditions: beam current of 10 nA; acceleration voltage of 15 kV; beam diameter of 3 μm; analyzed elements: B, F, Na, Mg, Al, Si, Cl, K, Ca, Ti, Cr, Mn, Fe, and Ba. Chemical formulas were calculated on the basis of O_{20}(OH, F, Cl)$_4$ (micas), O_{10}(OH, F, Cl)$_4$ (chloritoid), $(CO_3)_2$ (carbonates), 19 cations including B (tourmaline), O_8 (feldspar), or O_4 (magnetite). The mineral abbreviations used in the article are from Whitney and Evans (2010).

^{40}Ar-^{39}Ar data were completed at IGG–CNR (Pisa, Italy), using both the laser step-heating and the laser in situ techniques. Data were first collected by step-heating experiments on white-mica separates (grain size 0.25–0.35 mm) obtained through standard separation techniques. In situ analyses were carried out at a later time on rock chips ~8.5 mm in diameter drilled from polished thick sections (~400 μm thick). Rock chips and the mineral separates, after cleaning by alternating methanol and deionized water, were wrapped in aluminum foil and irradiated along with the Fish Canyon Tuff sanidine (FCs) in the core of the TRIGA reactor at the University of Pavia (Italy) in two distinct batches, for 30 hr (irradiation PAV-69) for step-heating analyses and for 60 hr (irradiation PAV-84) for samples analyzed by the in situ technique. Argon isotope compositions were determined using either a MAP215-50 single-collector noble gas mass spectrometer (irradiation PAV-69) or an ARGUS VI (Thermo Fisher Scientific) multicollector mass spectrometer (irradiation PAV-84). The neutron fluence was monitored by analyzing grains of the FCs, which were melted using a continuous wave CO_2 laser (New Wave Research MIR10–30 CO_2 laser system). Laser step-heating experiments were performed on white-mica separates using a diode-pumped Nd:YAG infrared (IR) laser beam, defocused to a ~2 mm spot size and homogenized by a beam-homogenizer lens. Steps were carried out at an increasing laser power until complete melting. In situ ^{40}Ar-^{39}Ar analyses were mainly completed through an ultraviolet (UV) laser beam, produced by a pulsed flashlamp Nd:YAG laser (frequency quadrupled and Q-switched). The UV laser, operating at 20 Hz and 0.5–1 mJ per pulse, was focused to ~10 μm and repeatedly rastered, by a computer-controlled *x*–*y* stage, over

areas of ~0.009–0.012 mm^2 (typically ~100 × 100 μm) and a few 10 μm deep. In situ ^{40}Ar-^{39}Ar analyses were also carried out using single laser shots (lasting 20–30 ms each) of the Nd:YAG laser operating at ~15 W, and focused to produce melt pits ~100–150 μm in diameter. The IR laser spot fusion technique was locally preferred over the UV laser ablation where, due to the fragility of some microdomains in sample R1b, the mica packets tended to shatter during sampling with the UV laser. Argon isotope compositions for irradiation PAV-69 were acquired by peak jumping through a single-collector noble gas mass spectrometer MAP215-50, fitted with a secondary electron multiplier. Gas purification (10 min, including ~2 min of lasering) was achieved by two SAES AP10 GP MK3 getters held at 400°C, one SAES C-50 getter held at room temperature and a liquid nitrogen cold trap. Blanks were analyzed every three to four analyses. A polynomial function was fit to the blanks analyzed during the day of acquisition, and unknown analyses were corrected based on the time of measurement. Line blank variation is given in Table S2. More details about mass spectrometer analysis can be found in Di Vincenzo and Skála (2009). Argon isotope compositions for irradiations PAV-84 were instead acquired simultaneously through a multicollector noble gas mass spectrometer ARGUS VI. Ar isotopes from 40 to 37 were acquired using Faraday detectors, equipped with 10^{12} Ω resistors for ^{40}Ar and ^{38}Ar and 10^{13} Ω resistors for ^{39}Ar and ^{37}Ar. Faraday detectors were cross-calibrated for the slight offset using air shots. ^{36}Ar was measured using a Compact Discrete Dynode (CDD) detector. Gas purification (4 min, including ~3 min of lasering) was achieved using three SAES NP10 getters (one water cooled, held at ~400 C and two at room temperature). Blanks were monitored generally every two runs and were subtracted from succeeding sample results. Line blank variation is given in Table S2. More details about mass spectrometer calibration and analysis can be found in Di Vincenzo et al. (2021). The correction factors for interfering isotopes from K and Ca were determined on K-rich and Ca-rich glasses and are listed in Table S2. Ages were calculated using decay constants recalculated by Min et al. (2000), an atmospheric ^{40}Ar-^{36}Ar ratio of 298.56 ± 0.31 (Lee et al., 2006) and an age of 28.201 ± 0.046 Ma for the FCs (Kuiper et al., 2008). Data corrected for postirradiation decay, mass discrimination effects, and blank are listed in Table S2. Uncertainties on single runs are 2σ analytical uncertainties, including in-run statistics and uncertainties in the discrimination factor, interference corrections, and procedural blanks. Uncertainties on the total gas ages and on error-weighted means also include the uncertainty on the fluence monitor (2σ internal errors). Cumulative probability plots and deconvolution of multiple age components for in situ data were realized using the Isoplot/Ex program, v. 3.75 (Ludwig, 2012).

4. Results

4.1. Sample Descriptions, and Microstructural and Microchemical Data

We investigated five representative samples (three from the Massa Unit and two from the Apuane Unit) that were selected among a set of more than 150 specimens collected from the metasedimentary successions. We purposely avoided rock samples from the Paleozoic basement, in order to reduce the probability of encountering prealpine mineralogical relicts. The choice was guided by the presence of well-developed and sufficiently thick phyllosilicate-rich layers and the occurrence of different foliations with clear overprint relationships. Additionally, all selected samples have been collected from areas that were well-known from a structural point of view, with unambiguous overprinting relationships (Carmignani & Kligfield, 1990; Molli, Conti, et al., 2000; Molli & Meccheri, 2012). Figure 2 illustrates, through geological cross-sections, the framework of the studied samples and their large (kilometer) to small (decimeter) scale relationships with the main interfering fold structures.

4.1.1. Massa Unit

Samples 22, 265, and R1b are part of the Triassic metasedimentary sequence of the Massa Unit. They were collected in two different sectors, toward the northernmost (22 and 265) and the southernmost (R1b) terminations of the unit (Figure 1).

Sample 22 is part of the Mt. Brugiana sequence, which includes Ladinian carbonate-platform deposits with marbles, calcschists/impure marbles, and metabreccias, formed of marble clasts within a phyllosilicate-rich matrix (Martini et al., 1986; Patacca et al., 2011). Sample 22 is a metabreccia, which is characterized by a continuous to spaced schistosity, defined by phyllosilicate layers distributed within a calcite and quartz-rich fine-to coarse-grained matrix. Locally, a phyllosilicate-rich millimeter-thick compositional layering may be recognized, in which the main foliation can be classified as differentiated crenulation (Figures 2 and 4a–4c), thus documenting

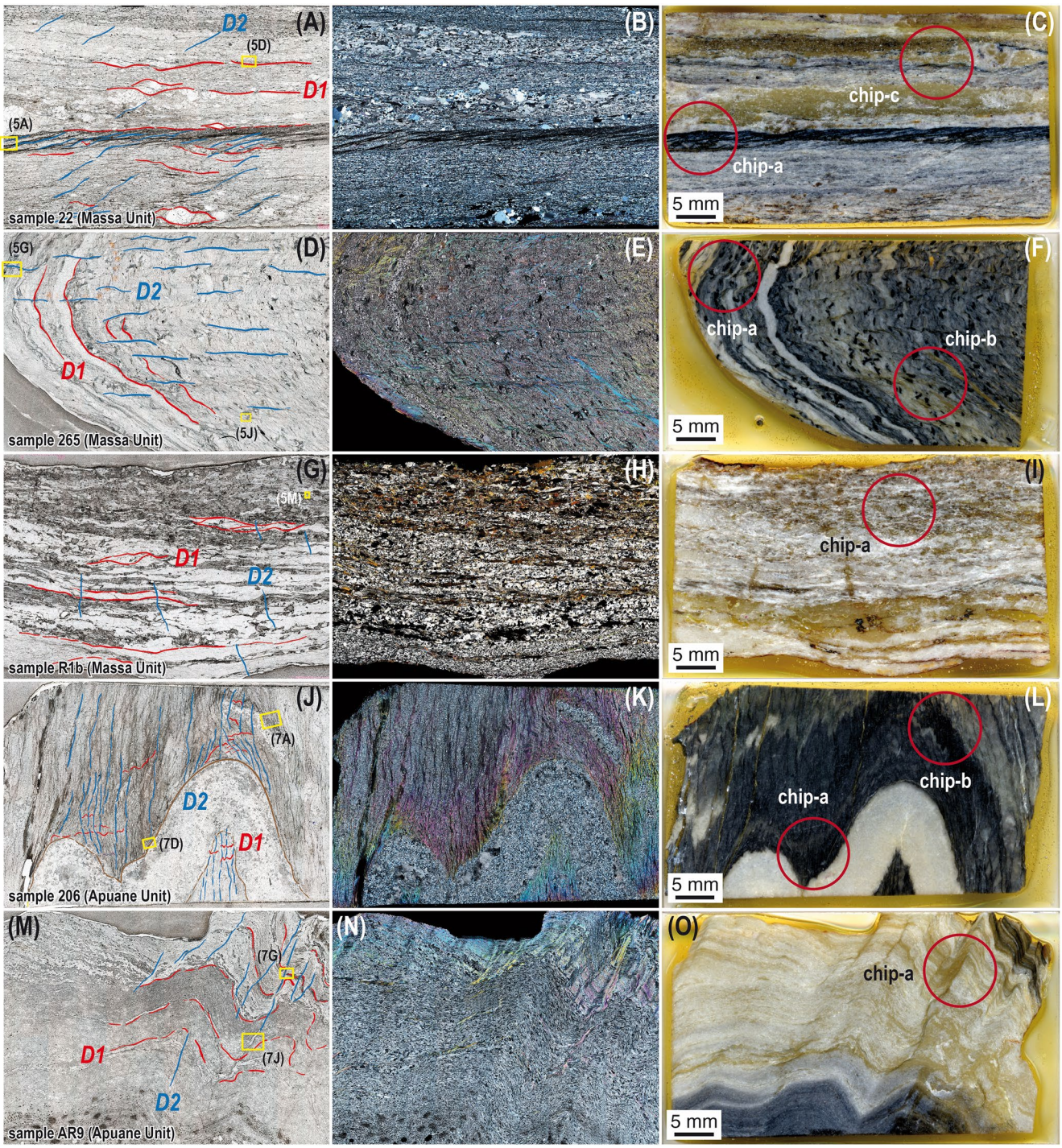

Figure 4. Microstructures of the samples investigated in the present study. (a, d, g, j, and m) thin sections under plane-polarized light. (b, e, h, k, and n) thin sections under cross-polarized light. (c, f, i, l, and o) photographs of the thick slices, counterfaces of sections; red circles indicate the drilled rock chips used for in situ ^{40}Ar-^{39}Ar dating. (a–c) sample 22 from the Massa Unit; (d–f) sample 265 from the Massa Unit; (g–i) sample R1b from the Massa Unit; (j–l) sample 206 from the Apuane Unit; and (m–o) sample AR9 from the Apuane Unit. D1 and D2 highlight the two foliations present in all the samples examined. The yellow rectangles in (a, d, g, j, and m) indicate the position of the areas imaged by SEM and shown in Figures 5 and 7.

the composite origin of the main D1 foliation. The D1 foliation is crenulated by a D2 discrete millimeter-spaced foliation, characterized by a reorientation/recrystallization of previous phyllosilicates associated with recrystallization of fine-grained white micas. The spacing and orientation of the D2 crenulation are compositionally controlled, being narrower and steeper in phyllosilicate-rich layers compared to the quartz-rich layers, as a result

of D2 strain partitioning and cleavage refraction. Sample 22 is mainly made up of quartz, phengite often associated with some paragonite, clinozoisite, calcite, and accessory minerals such as magnetite, ilmenite, tourmaline, and apatite (Figures 5a–5f). A phyllosilicate-rich layer at the center of the sample (see Figures 4a–4c), more pelitic in composition, is rich in micas and lacks calcite and clinozoisite (Figures 5a–5f). The deformation within this layer is more penetrative, with a D1 schistosity strongly reworked by a differentiated D2 crenulation. Relative to the other samples from the Massa Unit, the phengite of sample 22 shows a stronger celadonite substitution (Figure 6: blue triangles; Si = 6.322 ± 0.082 (±1σ) atoms per formula unit (apfu); X_{Mg} = Mg/[Mg + Fe^{2+} + Mn] = 0.412 ± 0.034) and a heterogeneity that results in a clear dispersion of the analyses in the diagrams of Figure 6 but it is hardly visible in Figure 5 (slight variations in grays and colors in Figures 5a and 5b, respectively). While these phengite flakes are mainly concentrated parallel to the D1 schistosity, much of the paragonite lately grew parallel to the D2 crenulation schistosity (Figures 5b and 5c). Replacement of potassic white mica by paragonite is more pervasive in the phyllosilicate-rich layer with respect to the calcite and quartz-rich matrix (Figures 5a–5c vs. 5d–5f).

Sample 265 (Figures 4d–4f) can be referred to as the Carnian Verrucano sedimentary cycle (Patacca et al., 2011), which includes green to purple metapelites and metasiltites associated with metaconglomerates characterized by the occurrence of pinkish quartz pebbles and tourmalinites ("anagenites" of the old literature—see Conti et al., 2020 and references therein). Sample 265 is a chloritoid-bearing schist in which a millimeter spaced quartz-rich compositional layering and a subparallel continuous D1 foliation is folded into a close centimeter-scale D2 fold (Figure 4d). A millimeter-spaced crenulation cleavage defines the axial planar D2 foliation with the millimeter long chloritoid laths observable as pretectonic porphyroblasts. The subhorizontal D2 crenulation is the axial planar foliation of a hectometer-scale fold (Figure 2) affecting the two juxtaposed Massa and Apuane units, and therefore constraining the relative timing of the thrusting of the Massa on top of the Apuane Unit (Molli, Giorgetti, & Meccheri, 2000). Quartz, phengite, paragonite, and chloritoid are the main minerals in sample 265, which additionally contains microcrystals of rutile, apatite, and tourmaline. The chloritoid occurs as millimeter-sized porphyroblasts, with a pronounced zonation (Figure 5k), consisting of an increase in X_{Mg} from the core to the mantle (X_{Mg}: 0.17 → 0.29) and then a decrease at the edge of the crystals (X_{Mg} → 0.20), which seems to reflect the prograde and retrograde evolutions of the rock. Some microinclusions of muscovite, quartz, tourmaline, and titanomagnetite are visible in these porphyroblasts and would belong to an early paragenesis. The matrix is mainly made up of quartz, phengite, and paragonite, which define the D1 schistosity, reworked by the D2 crenulation. Paragonite is intimately associated with phengite in microlayers of micrometer-sized crystals aligned along the schistosity (Figures 5g–5l), preventing the separate analyses of the two minerals (violet diamonds in Figure 6 are mixtures of phengite and paragonite). Locally, a phengitic muscovite, little substituted in celadonite (Figure 6: violet triangles; Si = 6.103 ± 0.042 apfu), forms flakes tens of micrometers thick and hundreds of micrometers long with a nearly homogeneous composition, which seem preferentially concentrated on the D1 schistosity.

Sample R1b is part of the Mt. Folgorito Formation, a fining- and deepening-upward sequence of alluvial metaconglomerates and metasandstones of Middle Triassic age (Anisian-Ladinian, Patacca et al., 2011). R1b is compositionally a quartz-rich schist, consisting of quartz, kyanite, and white micas, and characterized by a millimeter-spaced zonal schistosity D1, with alternating quartz-rich and phyllosilicates-rich domains (Figures 4g–4i). The local presence of relict domains with microfolded white micas documents the composite origin of the main foliation D1, in agreement with microtextural and microchemical data that will be presented below. The R1b sample shows a very week overprint of the D1 composite fabric by a D2 disjunctive crenulation cleavage. Sample R1b is mainly formed of crystals of quartz, kyanite, and white micas, aligned along the main schistosity (Figures 4g–4i and 5m–5o). White mica, a phengitic muscovite poorly substituted in celadonite (Figure 6: green triangles; Si = 6.038 ± 0.066 apfu), appears to be preferentially concentrated between quartz and kyanite (Figure 5n). Close to the contact with kyanite, muscovite flakes show irregular and discontinuous rims of late paragonite up to few tens of micrometer thick (Figure 5n), which cannot be analyzed separately because they are finely intergrown with muscovite (green diamonds in Figure 6 are mixtures of Ms + Pg). Some microcrystals of rutile, tourmaline, apatite, and svanbergite, a rare phosphate of some aluminous metamorphic rocks, are included in quartz, muscovite, and kyanite crystals, where they are aligned according to an early schistosity (Figures 5m and 5n).

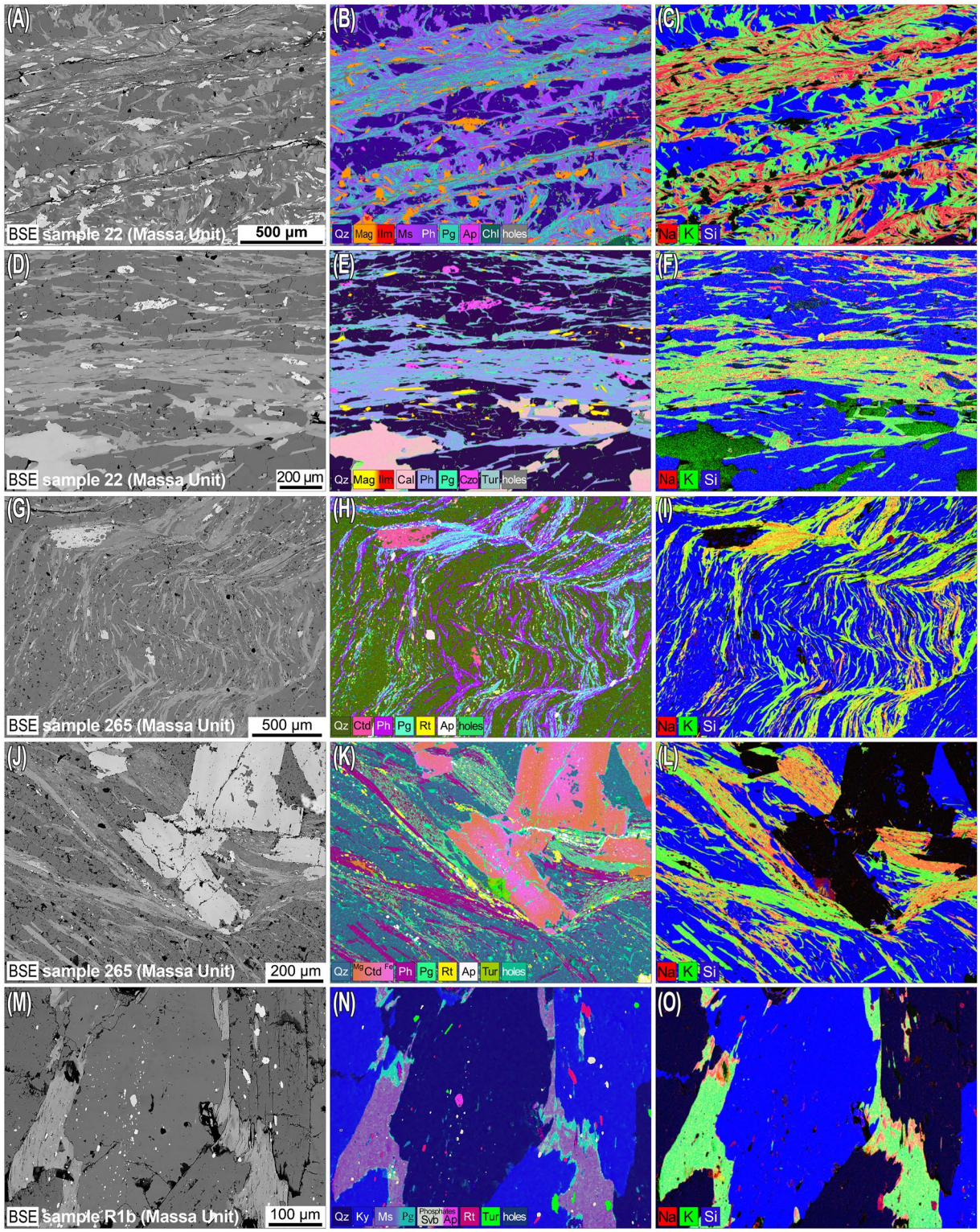

Figure 5. Mineralogy and microstructures of the studied samples from the Massa Unit. Samples 22 (a–f), 265 (g–l), and R1b (m–o). (a, d, g, j, and m) BSE images; (b, e, h, k, and n) images combining the first three principal components that result from the principal component analysis (PCA) of 10 chemical maps; and (c, f, i, l, and o) images combining the chemical maps of Na (red), K (green), and Si (blue).

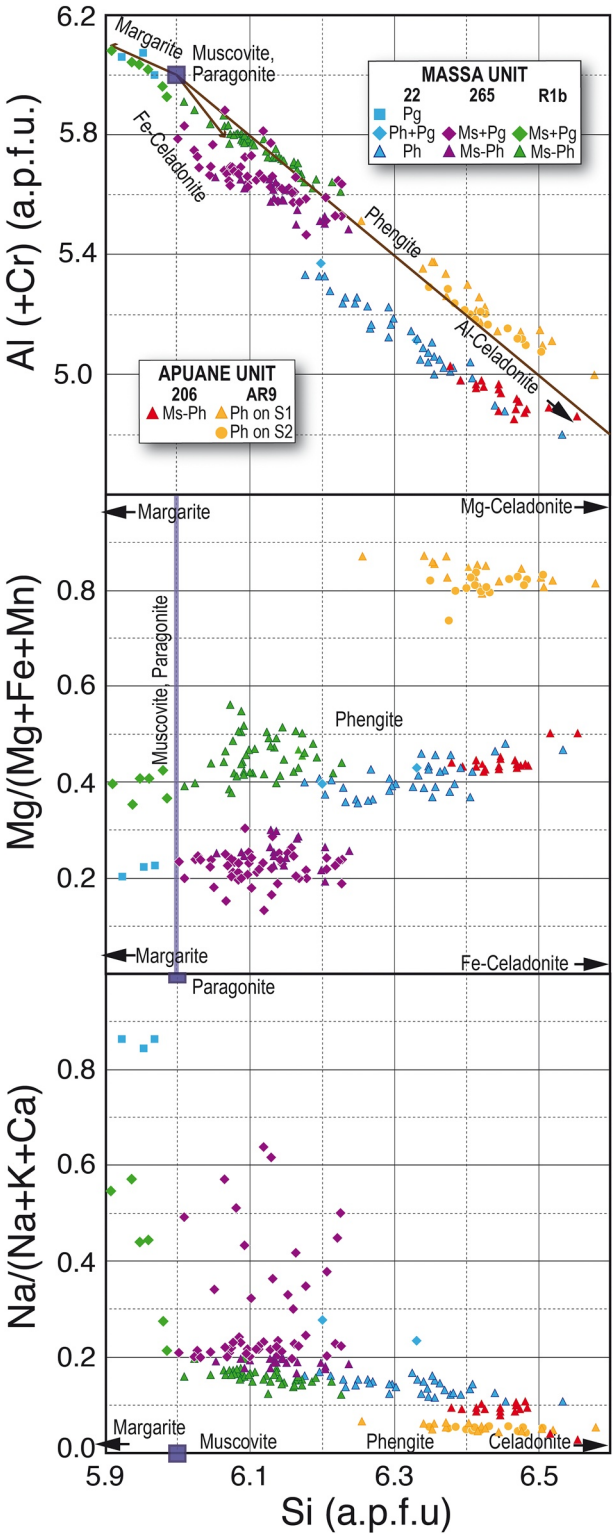

Figure 6. Electron microprobe (EMP) data of the white micas (Al vs. Si; X_{Mg} vs. Si; and X_{Na} vs. Si). X_{Mg} = Mg/(Mg + Fe + Mn) and X_{Na} = Na/(Na + K + Ca). Ph + Pg means physical mixture of micrometer-sized crystals of phengite and paragonite and Ms-Ph means solid solution varying between muscovite and phengite compositions.

4.1.2. Apuane Unit

Samples 206 and AR9 are from the Apuane Unit and are representative of its westernmost and easternmost zones, respectively (Figure 1). The protolith of sample 206 is referable to the Scisti Sericitici Formation, which is a metamorphic equivalent within the Apuane Unit of the Cretaceous-Tertiary pelagic Scaglia Formation of the Tuscan sequence (Conti et al., 2020). Sample 206 is a phyllosilicate, carbonates, and quartz-bearing slate, characterized by a continuous cleavage folded in close to tight centimeter-scale folds, which are revealed by a centimeter-thick quartz-dolomite-calcite folded vein. The axial planar foliation of the microfolds is highlighted by a millimeter-spaced, discrete, smooth, and parallel crenulation cleavage D2 (Figures 4j–4l). Sample 206 consists of white mica, quartz, dolomite, calcite, and the accessory minerals magnetite, rutile, apatite, and tourmaline (Figures 7a–7f). White mica, a phengite highly substituted in celadonite (Figure 6: red triangles; Si = 6.451 ± 0.042 apfu; X_{Mg} = 0.443 ± 0.022), defines with quartz and dolomite the D1 schistosity. It has evolved without any noticeable change in composition parallel to the cleavage planes of crenulation D2, enhanced by magnetite microcrystals (Figure 7e). While this phengite is concentrated in the matrix, the centimeter-thick vein folded by D2 is essentially made up of quartz, calcite ($Cal_{95}Mgs_2Sd_1Rds_3$), and dolomite with a significant Fe-content ($Cal_{51}Mgs_{36}Sd_{10}Rds_3$).

The protolith of sample AR9 is attributable to the Late Jurassic Marble Formation, which includes the eastern Alpi Apuane widespread marbles and breccias, and impure marbles (Conti et al., 2020). Sample AR9 is a carbonate- and quartz-bearing calcschist, showing a millimeter-scale compositional layering (Figures 4m–4o), with alternating pelitic (Figures 7g–7i) and carbonate (Figures 7j–7l) microlayers derived from the original bedding and a subparallel continuous D1 schistosity. Layering and D1 schistosity are folded into close to tight centimeter-scale microfolds, the axial plane of which is underlined by a millimeter-spaced, discrete smooth, and parallel D2 crenulation cleavage, well-developed in the phyllosilicate-rich domains (e.g., Figure 7g). Sample AR9 is quite similar to sample 206 but richer in carbonates. It shows an inherited layering (Figure 4m) with alternating pelitic (Figures 7g–7i) and carbonate (Figure 7j–7l) layers, affected by D1 schistosity and D2 crenulation (e.g., Figures 4m–4o and 7g). Phengite, highly substituted in Mg-celadonite (Figure 6: brown symbols; Si = 6.434 ± 0.089 apfu; X_{Mg} = 0.826 ± 0.027), does not show any notable variation depending on whether it is parallel to the D1 and D2 schistosities (Figure 6: yellow triangles and circles, respectively). Among the carbonates, calcite dominates ($Cal_{97}Mgs_2Sd_1Rds_2$) and dolomite have a slightly variable amount of Fe ($Cal_{51}Mgs_{43\pm3}Sd_{6\pm3}Rds_0$).

4.2. ^{40}Ar-^{39}Ar Data

4.2.1. Step-Heating Data on White-Mica Separates

A few milligrams of white-mica separates from the five selected samples were laser step-heated and analyzed using a single collector noble gas mass spectrometer. All white micas from both units gave variably discordant age spectra, with overall sigmoidal shapes (Figure 8). However, three out of the five samples analyzed (samples 22, 206, and AR9) yielded a concordant segment representing more than 50% of the total $^{39}Ar_K$ released (Figure 8). The age spectrum of white mica from sample 22 (Massa Unit), after a first step at ~20 Ma, is characterized by an increasing age spectrum (from 9.3

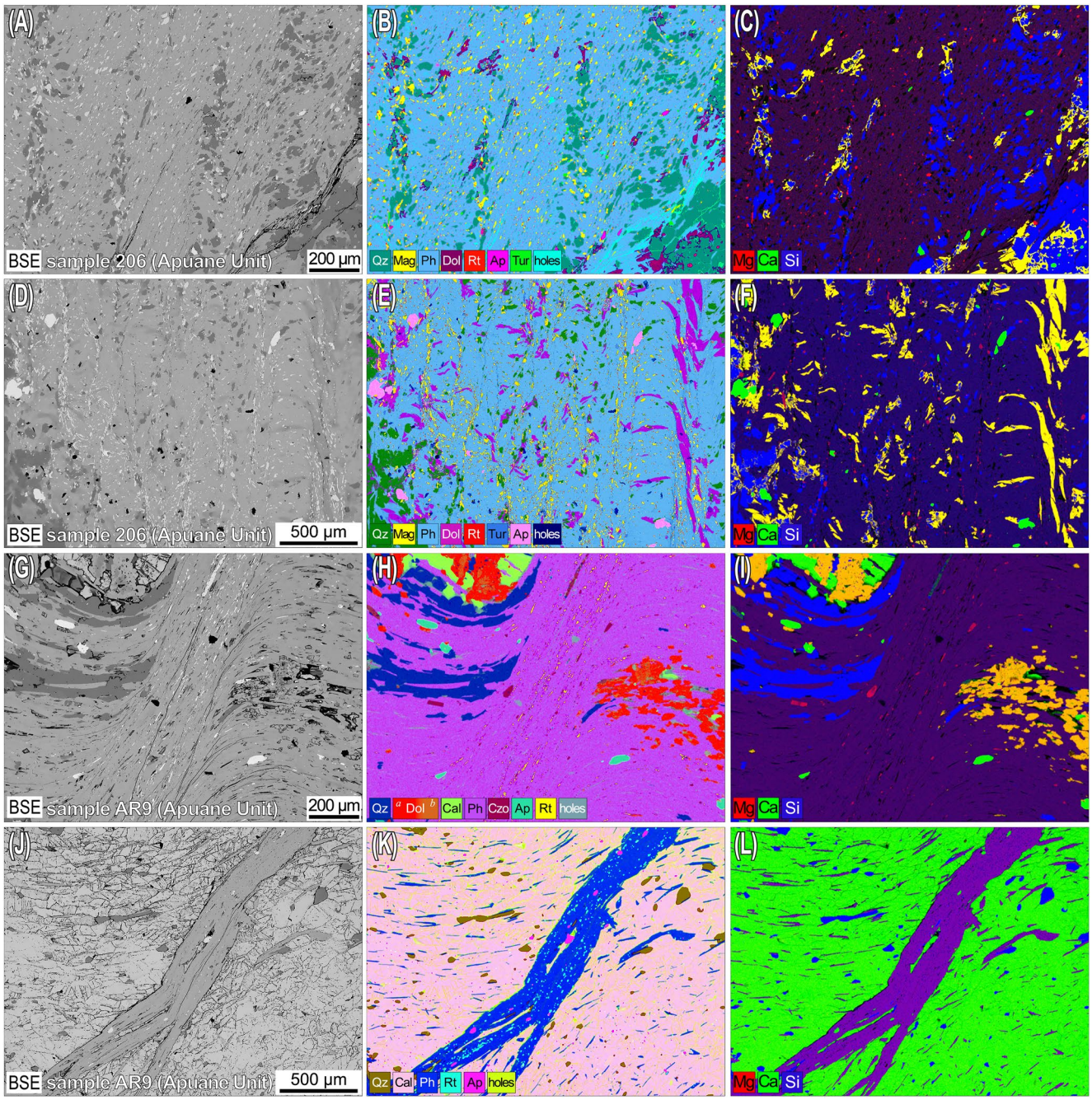

Figure 7. Mineralogy and microstructures of the studied samples from the Apuane Unit. Samples 206 (a–f) and AR9 (g–l). (a, d, g, and j) BSE images; (b, e, h, and k) images combining the first three principal components that result from the PCA of 10 chemical maps; and (c, f, i, l) images combining the chemical maps of Mg (red), Ca (green), and Si (blue).

to 10.5 Ma), followed by seven consecutive steps indistinguishable within the analytical uncertainties (MSWD 2.03, probability 0.06) and representing 50.9% of the total $^{39}Ar_K$ released, yielding a weighted-mean age of 11.74 ± 0.17 Ma. The final three steps gave increasing dates, up to ~30 Ma. The total gas age is 11.90 ± 0.15 Ma, slightly older than the mean age from the concordant segment. White-mica separate from sample 265 (Massa Unit), gave a similar age spectrum as that of sample 22, with a concordant segment representing ~30% of the total $^{39}Ar_K$ released and yielding a weighted mean age of 15.33 ± 0.18 Ma, close to the total gas age of 15.66 ± 0.16 Ma. The final ~30% of the total $^{39}Ar_K$ released gave increasing step ages up to ~48 Ma (Figure 8a). The sigmodal shaped age spectrum of sample R1b (Massa Unit) lacks a significant concordant segment at

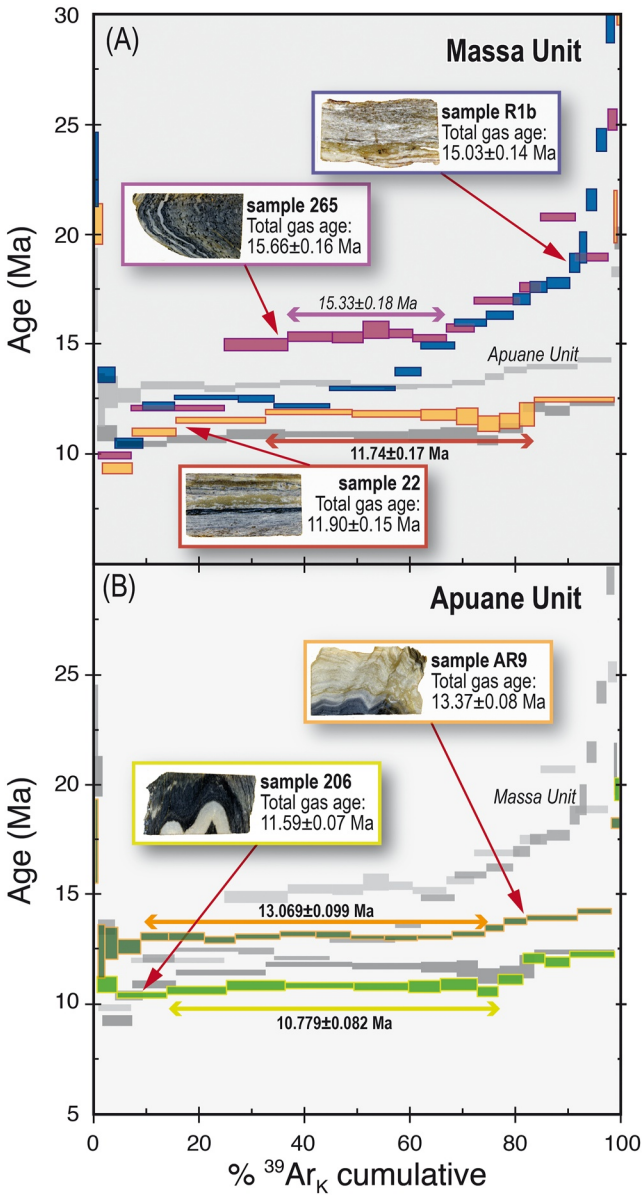

Figure 8. ^{40}Ar-^{39}Ar age spectra from step-heating analysis on white-mica separates. Data were acquired in peak-jumping mode through a single-collector noble gas mass spectrometer. (a) Data from samples of the Massa Unit. (b) Data from samples of the Apuane Unit. Box eight corresponds to 2σ analytical uncertainties. Uncertainties given for total gas and weighted-mean ages are 2σ and also include the uncertainty in the flux monitor.

intermediate temperatures and is characterized by a staircase segment for more than 50% of the total $^{39}Ar_K$ released, with step ages ranging from 12.2 to ~41 Ma and a poorly defined final step with an age of 148 ± 6 Ma. The total gas age is 15.03 ± 0.14 Ma (Figure 8a).

The white micas from the two samples of the Apuane Unit gave less disturbed age spectra compared to those of the white micas from the Massa Unit (Figure 8b). In sample 206, more than 98% of the total $^{39}Ar_K$ released gave step ages scattering within a relatively narrow range of 10.4–12.2 Ma, with a concordant segment (more than 60% of the total $^{39}Ar_K$ released) yielding a mean age of 10.779 ± 0.082 Ma (Figure 8b). The total gas age is 11.591 ± 0.070 Ma. Similarly, white mica of sample AR9 yielded step ages, representing ~98% of total $^{39}Ar_K$ released, scattering within ~2 Ma, in between 12.3 and 14.2 Ma (Figure 8b). Ten consecutive steps representing ~65% of the total $^{39}Ar_K$ released gave a weighted-mean age of 13.069 ± 0.099 Ma, slightly younger than the total gas age (13.370 ± 0.080 Ma).

4.2.2. In Situ Data on Rock Chips

In situ UV laser-ablation and IR laser spot-fusion analyses are listed in Table S2 and presented in the frequency diagrams along with the cumulative probability plots of Figure 9. In addition, data for selected areas are reported in Figure 10 to illustrate the intrasample distribution of Ar isotopes. The two rock chips investigated in sample 22 (Massa Unit) gave ages mainly within a narrow interval from ~9.7 to ~13.3 Ma (Figure 9a), with the exception of one spot date characterized by a low K/Ca ratio (0.7 ± 0.1, derived from neutron-produced $^{39}Ar_K$ and $^{37}Ar_{Ca}$ isotopes—Table S2) that is suggestive of contamination by a high-Ca and low-K mineral phase and yielding a very old Upper Eocene date (~35 Ma). Only three spot ages from Chip-B, yielding Burdigalian dates, exceed the range mentioned above, one of which is, however, characterized by again a low K/Ca ratio (~0.03 – Table S2), incompatible with an analysis completed on a pure white mica. It is important to note that fifteen of the eighteen data completed in the millimeter-thick pelitic layer of Chip-A (Figure 10d) gave ages indistinguishable within analytical uncertainties, with a mean age of 10.486 ± 0.092 Ma (MSWD 0.78). A single date, slightly but significantly younger than the weighted mean, is also from the pelitic layer of Chip-A (analysis 81D, age 9.7 ± 0.3 Ma—Figure 10d and Table S2) but it shows a negative ^{36}Ar content after blank correction and is therefore considered unreliable. Data from the calcite-quartz matrix generally yield older ages, mainly within ~11–12.5 Ma. Chip-C exhibits an age variation similar to that of Chip-A, eleven out of the twenty eight laser pits yield ages matching the mean age of ~10.5 Ma (pooled weighted mean of 10.566 ± 0.092 Ma—MSWD 1.47 and probability 0.06), although the data for the thinner mica layer of Chip-C are more variable with respect to the mica layer of Chip-A (Figures 10a and 10c). Sample 265 (Massa Unit) gave similar age variations for the two rock chips investigated (Figures 9b and 10e–10h), extracted from the hinge (Chip-A) and the flank (Chip-B) of the centimeter-sized fold included in the thick section, ranging mainly from ~11.2 to ~19.3 Ma (68 out of the 75 laser pits analyzed), with a nearly continuous variation. The fourteen youngest dates in Chip-A overlap within analytical uncertainties, with a weighted mean age of 11.84 ± 0.17 Ma (MSWD of 0.88), which is in close agreement with the mean age of 11.96 ± 0.16 Ma (MSWD of 1.53) derived from the fifteen youngest ages of Chip-B (pooled weighted mean of 11.91 ± 0.11 Ma—MSWD 1.22 and probability 0.19). In a cumulative probability plot of Ar ages from both rock chips (Figure 9b), the major peaks are all younger than the Burdigalian (<16.0 Ma). Five laser pits from Chip-A and four from Chip-B yield ages within the Burdigalian (16.0–20.4 Ma), and four from Chip-A and two from Chip-B are older (up to 61.7 Ma for Chip-A and as old as 37.4 Ma for Chip-B—Figure 9b and Table S2). Burdigalian or older ages are more commonly associated with

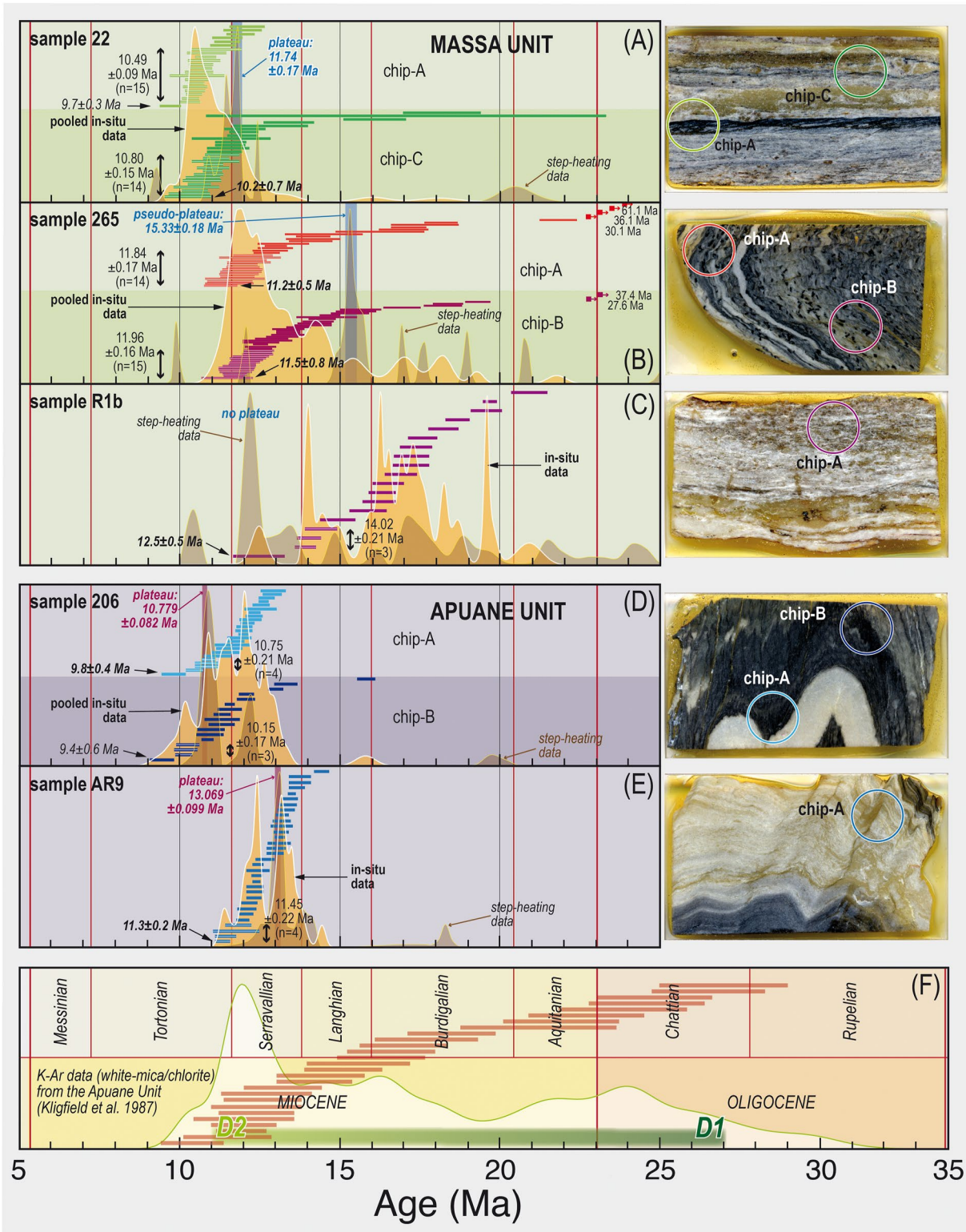

Figure 9. Summary of in situ ^{40}Ar-^{39}Ar data on rock chips: cumulative probability distribution and ranked distribution. The ranked distribution of ages is given for each rock chip investigated together with the youngest age and the mean of the youngest statistically indistinguishable dates. A pooled cumulative probability distribution was calculated when two rock chips were investigated for the same sample (a, b, and d). Cumulative probability curves for step-heating data are shown for comparison. (a, b, and c) data from samples of the Massa Unit. (d and e) data from samples of the Apuane Unit. The timescale in (f) also includes for comparison available K-Ar data for the Apuane Unit (Kligfield et al., 1986). In situ laserprobe data were acquired by a multicollector noble gas mass spectrometer. Uncertainties are 2σ.

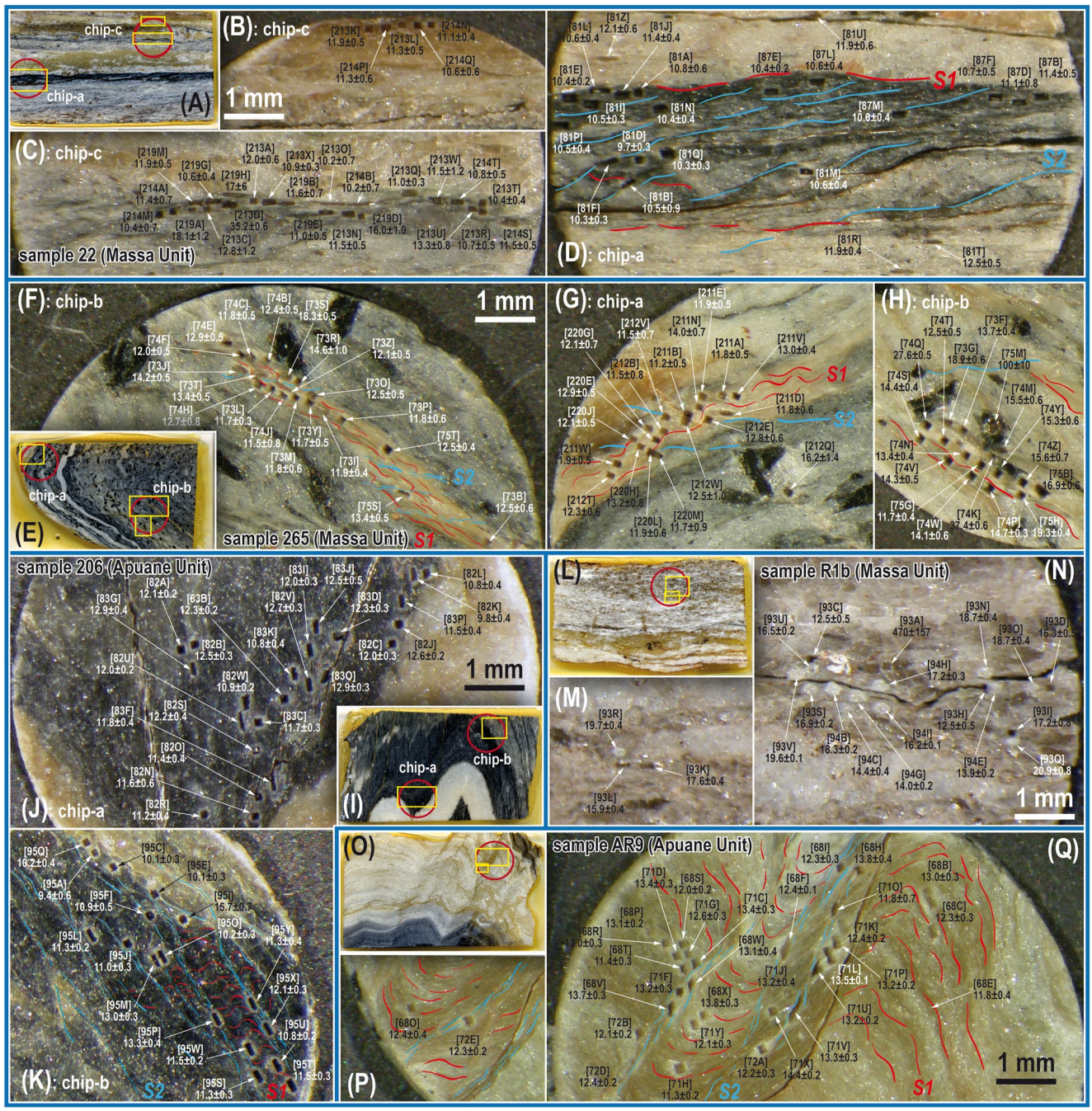

Figure 10. Age mapping of selected areas from the rock chips investigated by the Ar laserprobe. Numbers for each analysis refer to those listed in Table S2. Ages are in Ma followed by ±2σ analytical uncertainties. (a–d) sample 22 from the Massa Unit. (e–h) sample 265 from the Massa Unit. (i–k) sample 206 from the Apuane Unit. (l–n) sample R1b from the Massa Unit. (o–q) sample AR9 from the Apuane Unit. S1 (D1) and S2 (D2) highlight the two foliations present in all the samples examined. Most analyses were completed through an UV laserprobe (laser ablation). A few analyses in sample R1b were realized using an IR laserprobe (spot fusion) and appear as whitish circles (n).

chloritoid-bearing domains (Figures 10f–10h). In situ ^{40}Ar-^{39}Ar data from white mica defining the micaceous, thicker, and crenulated continuous layers show a patchy age distribution, with the youngest ages not necessarily located along the younger crenulation cleavage domains (Figures 10f and 10g). Two analyses carried out in the chloritoid gave anomalous old ages, even exceeding in one case the time of the sedimentary protolith, suggesting the presence of excess argon (parentless ^{40}Ar) hosted in chloritoid. Sample R1b (Massa Unit) yielded a significantly different age distribution when compared to the previous two samples of the same unit, both in terms of

dates and dispersion (Figure 9c). ^{40}Ar-^{39}Ar data from white mica, after a young age of ~12.5 Ma, gave a nearly smooth and continuous distribution of dates from ~14 to ~21 Ma, with a maximum distribution of ages within the Burdigalian but without a discernable dominant peak. In this sample, due to the general whitish appearance of the thick section and the lack of dark minerals, the microstructural and microtextural control on the positioning of the laser pits were more complicated with respect to the previous samples. The age mapping reveals a rather patchy distribution (Figure 10l–10n).

In sample 206 (Apuane Unit), two rock chips were investigated, one (Chip-A) located in between the two centimeter-sized folds included in the thick section and the second from the hinge of the larger fold (Chip-B) (Figure 9d). Data from the two rock chips gave similar age variations, with ages ranging from ~9.8 to 13.3 Ma, with an almost continuous variation (Figure 9d). A younger age (~9.4 Ma) in Chip-A is considered inaccurate because of negative ^{36}Ar after blank correction. One laser pit in Chip-B gave a significantly older date of ~15.8 Ma (95I, Table S2) but it is characterized by a low K/Ca ratio (~0.28) and it is therefore considered unreliable. The youngest date from Chip-A is 9.8 ± 0.4 Ma and is followed by four concordant ages with a mean of ~10.8 Ma in Chip-A and three concordant ages with a mean of ~10.2 Ma in Chip-B. The pooled cumulative probability curve for the two rock chips exhibits several peaks within the 9.8–13.3-Ma range, more specifically at ~10.1, 10.9, 11.5, 12.0, and 12.7 Ma. Age mapping reveals no age variation between white micas aligned along the D1 and D2 schistosities but a rather patchy distribution (Figures 10i–10k). In situ ^{40}Ar-^{39}Ar analyses of sample AR9 (Apuane Unit) gave a nearly continuous variation of dates, from ~11.3 to ~14.4 Ma, which largely overlap with the interval defined by sample 206 but with an older minimum age limit (Figure 9e). The youngest four analyses yield ages overlapping within uncertainties, with a weighted mean age of 11.45 ± 0.22 Ma. In a cumulative frequency plot, the data show discernable peaks at ~11.4, 12.3, 13.1, 13.5, and 14.4 Ma. Once again, the age mapping does not reveal any systematic variation between white micas aligned along the D1 and D2 schistosities (Figures 10o–10q).

5. Discussion

5.1. Interpretation of ^{40}Ar-^{39}Ar Data and Timing of Deformation in the Alpi Apuane

All investigated samples from both units exhibit a significant internal scatter of in situ Ar ages and variably discordant age spectra from step-heating data, which attest to a pronounced intrasample Ar isotope disequilibrium. This dispersion is paralleled by the development of paragonite after muscovite/phengite in samples from the Massa Unit, which implies the mobility of alkalis (see below), but has no obvious counterpart in the much less evident compositional variation of white mica in samples from the Apuane Unit. Based on (a) the microstructural and microchemical features presented above, (b) the pronounced intrasample isotope disequilibrium observed in all samples investigated and testified by both ^{40}Ar-^{39}Ar in situ data on rock chips and step-heating on bulk mineral separates, and (c) the available *P-T* estimates and paths from the literature, we infer that syn-deformation white mica growth and recrystallization took place under temperature conditions (<500°C) at which volume diffusion produces negligible effects on the Ar isotope record that is at temperatures under which the rate of dissolution/reprecipitation processes far exceeds that of volume diffusion (Di Vincenzo et al., 2004; Villa et al., 2014; Villa & Hanchar, 2017). Empirical evidence from natural examples has been recently strengthen by a revaluation of the ^{40}Ar diffusion dependence to temperature via atomistic simulations (Nteme et al., 2022), which gave diffusive parameters that, for cooling rates ranging from 1 to 100°C/Ma and grain sizes varying between 0.1 and 1.0 mm, yield closure temperatures in the range of 560–800°C, close to the upper stability limit of muscovite.

The three metapelitic samples from the Massa Unit studied here recorded several episodes of deformation, typically resulting in a D1 schistosity followed by a D2 crenulation. The occurrence of relict domains testifies to the composite nature of D1 deformation that is compatible with a protracted evolution over time. Importantly, the development of D2 crenulation was compositionally controlled, with spacing and orientation being narrower and steeper in the phyllosilicate-rich layers when compared to the quartz-rich layers. The D1 structures are only very weakly reworked by the D2 crenulation in the southern sample R1b but they are pervasively overprinted in the millimeter-thick pelitic layer of sample 22. In line with the above observations, the replacement of muscovite/phengite by paragonite was much more pervasive in the pelitic layer of sample 22, compared to the coexisting calcite- and quartz-rich layer or to the very local and discontinuous replacement along the rims of muscovite in sample R1b. The *P-T* stability field of paragonite in metapelites is quite wide, as it extends toward high

temperatures at most up to the univariant Pg + Qz = Ab + Als + H_2O curve, which has a positive *dP/dT* slope, with a concavity toward low *T* and high P (Figure 3). According to the *P-T* estimates available in the literature, this implies that paragonite may have been stable over the whole *P-T* path underwent by the Massa Unit, including during retrogression at upper crustal level. Microstructural data suggest that paragonite developed during the D2 deformation without growing at the expense of another preexisting sodic phase, such as albite, which is absent. Substitution of muscovite/phengite by paragonite (i.e., Ms + Na = Pg + K) may explain such a behavior, and this mechanism is strongly supported by the paragonite microcoronas formed around muscovite in sample R1b (Figures 5n and 5o). We therefore infer that the variable replacement of muscovite/phengite by paragonite occurred by fluid-assisted pseudomorphic replacement and was synchronous with the development of the D2 deformation. Nearly 90% of the total ^{40}Ar-^{39}Ar in situ data completed within the millimeter-thick pelitic layer of Chip-A from sample 22 gave homogeneous ages with a mean of 10.486 ± 0.092 Ma (Figure 10d), which matches remarkably the youngest dates found in the thinner pelitic layer of Chip-C (Figure 10c). Using the "Unmix-Ages" procedure of the Isoplot software (Ludwig, 2012), which allows to deconvolute a population of data containing multiple age components, the results from the two chips yield a mixture predominantly consisting of two components, one representing 56% of the whole population with an age of 10.54 ± 0.08 Ma and the other representing 34% yielding an age of 11.57 ± 0.16 Ma. Most of the ages falling at the Serravallian/Tortonian boundary (i.e., ∼11.6 Ma), are from the calcite-quartz matrix and overlap within uncertainty with the concordant segment of the step-heating data (11.74 ± 0.17 Ma) derived from the bulk white mica separate. The ages at the Serravallian/Tortonian boundary are also in line with the first discernable and highest peak defined by the thirty youngest in situ dates of sample 265, yielding a mean age of 11.95 ± 0.12 Ma. We therefore argue that samples 22 and 265 from the Massa Unit carry records of the development of D2 deformation, which was assisted by the introduction of Na-rich aqueous fluids, starting from at least the Serravallian/Tortonian boundary and ending in the middle Tortonian (at ∼10.5 Ma). This inference is supported by: (a) the asymmetry of the cumulative probability distribution of the in situ ages from samples 265 and 22, characterized by a marked steep flank at the young age side; (b) the similarity in age between the youngest dates in sample 265 and those from the calcite-quartz matrix of sample 22; (c) the age defined by the concordant segment of the step-heating data from sample 22, falling again at Serravallian/Tortonian boundary. Based on available data on muscovite-paragonite solvus (Guidotti et al., 1994), the K content accommodated in paragonite is expected to be low, with K/(K + Na) within 0.06–0.09 for temperatures ranging from 300 to 500°C, respectively. This would imply a reduction of the gas yield from the lasered volume consisting of pure paragonite by more than 10 times with respect to a phyllosilicate layer entirely consisting of muscovite/phengite. Such a significant drop of beam intensities, however, was not observed during the experimental work, reflecting the fact that the volume sampled by the laserprobe diffusely consisted of a microscale mixture of paragonite and muscovite/phengite (Figure 5), the latter being either relicts in the newly formed paragonite or, more likely, crystallized or reequilibrated during paragonite formation with the composition of coexisting micas defined by the paragonite-muscovite/phengite solvus. It is well known that the muscovite limb of the muscovite-paragonite solvus is shifted to lower X_{Na} ratios as phengitic substitution increases (e.g., Guidotti et al., 1994), which explains the slight negative slope of the muscovite-phengite compositional trend in the X_{Na} versus Si diagram of Figure 6 for at least two of the three samples (22 and R1b) from the Massa Unit. This in turn suggests that most of these K-rich micas have likely reached a state of equilibrium with the coexisting paragonite. It remains uncertain whether the deformation in the two samples with a prominent D2 fabric ended diachronically, that is, ∼1 Ma later in the southern sample (22) relative to the northern one (265) or whether this difference in ages is simply due to a weaker rheological behavior of the pelitic millimeter-thick layer investigated in sample 22.

The temporal constraints on the development of the D1 deformation remain on the contrary more uncertain, even using the data from sample R1b, in which the D2 deformation had very limited microstructural and microchemical effects. The oldest in situ ages from samples 22 and 265 mainly fall within the Burdigalian and are in line with most in situ ages from sample R1b (Figures 9a–9c). A few older ages (Priabonian-Rupelian or even older) from sample 265, typically associated with chloritoid-bearing domains, are of uncertain meaning as likely contaminated by excess Ar. Sample R1b yielded twelve out of nineteen dates within the Burdigalian, six younger (≥12.5 Ma) and one older (∼21 Ma). It is important to note that data exhibit a nearly continuous variation, with no discernable dominant peaks in the cumulative probability distribution, even on the older age side. This heterogeneity is paralleled by step-heating data, which gave an internally disturbed age spectrum, lacking reproducible step ages and with an overall staircase shape (Figure 8a). Unless we assume that the white mica R1b bears the

record of a dynamic (re)crystallization, which is in any case difficult to demonstrate, data may be solely used to constrain the minimum age for the onset of D1 deformation at the Aquitanian/Burdigalian boundary and a maximum age for the cessation of reequilibration during the D2 deformation at ∼12.5 Ma. Coincidentally, the latter age is close to the youngest in situ dates of sample 265 and to those from the calcite-quartz matrix of sample 22.

The two samples from the Apuane Unit show carbonate and pelitic centimeter-thick layers. The former are rich in calcite and dolomite, whereas the latter are dominated by phengite highly substituted in celadonite but without paragonite, in contrast to the samples from the Massa Unit. In both samples, the composition of phengite does not vary noticeably, irrespective of whether it is aligned along the D1 or D2 schistosities. The white-mica flakes of both samples show little evidence of internal strain, like kinking or grain segmentation with intragranular fractures, which may produce zones of high defect density and act as intragrain fast diffusion pathways (see e.g., Mulch et al., 2002). This suggests that white-mica flakes most likely resulted from syn-deformation growth and recrystallization that, in light of the small compositional variations, should have taken place under roughly similar *P–T* conditions or evolving parallel to the Si^{4+} isopleths of white mica (e.g., Beaudoin et al., 2020) and likely in a relatively short span of time. This hypothesis agrees with the quite limited scattering recorded by in situ analysis in both samples (Δt of 3.5 ± 0.5 and 3.1 ± 0.3 Ma for sample 206 and AR9, respectively) and with the limited disturbance of age spectra from step-heating analyses. Alternatively, white micas mostly reequilibrated during the D2 deformation and the scatter in age is due to the partial survival of pre-D2 relicts. Although in situ data from both samples define a relatively narrow range, it is significant and age mapping reveals that in both samples no systematic variations between white micas aligned along the D1 and D2 schistosities. The age distribution of sample 206, the most pelitic in composition, matches remarkably with that of Chip-A from sample 22 (Massa Unit), although with a more continuous variation, the five youngest ages yielding a mean of 10.2 ± 0.3 Ma, in close agreement with the 10.49 ± 0.09-Ma age from the pelitic layer of sample 22. The age distribution of sample AR9, richer in quartz and carbonates than sample 206, is rather more similar to that of sample 265 (Massa Unit), with the four youngest ages yielding a mean of 11.45 ± 0.22 Ma. Step-heating results conform to in situ data, with the concordant segment in sample 206 yielding a younger age (∼2.3 Ma younger) than that of sample AR9 (Figures 8 and 9), thus recalling the role of lithology on strain partitioning and, consequently, on the Ar isotope age record. It is important to note that both samples from the Apuane Unit gave in situ ages younger than the Langhian, with a single older date at ∼14.4 Ma in sample AR9. If on the one hand ^{40}Ar-^{39}Ar data from the Apuane Unit suggest a common temporal evolution with the Massa Unit for the development of D2 deformation, at least starting from the upper Serravallian, on the other hand the results allow us to constrain the minimum age for the onset of the D1 deformation in the Apuane Unit at the Langhian/Serravallian boundary, which is significantly younger (by ∼6.5 Ma) than the age derived from the Massa Unit. However, results from the present study do not clarify whether this difference arose from a true diachronism or simply from a more extensive reequilibration during the D2 deformation of the two samples investigated from the Apuane Unit.

5.2. Regional Implications

5.2.1. Comparison With Existing Geochronological Constraints

The first comprehensive geochronological investigation of deformation in the Alpi Apuane was presented by Kligfield et al. (1986). They reported a total of thirty-nine K-Ar ages on different size fractions (ranging from <0.6 μm to 6–20 μm) of white mica-chlorite mixtures and whole rocks from various lithologies of the Apuane Unit, with continental Triassic to shallow-water Verrucano-type deposits, and of phyllites from the Paleozoic basement of the Massa Unit. Twenty-seven K-Ar analyses of white mica-chlorite mixtures from cover rocks of the Apuane Unit (including slates, cherty schists, and calcschists) yielded ages in the range of ∼27.0–10.4 Ma, with a cumulative probability distribution characterized by a major peak at ∼12 Ma and minor peaks within 25–14 Ma (Figure 9f). Most of these K-Ar ages were younger than the Burdigalian, with five out of twenty-seven being Chattian. The latter were from samples characterized by an S1 foliation either uncrenulated or affected by a nonpenetrative or a penetrative D2 crenulation and collected from the northeastern sector of the Alpi Apuane (Gorfigliano and Arnetola areas, ∼7–4 km to the north of sample AR9 investigated in the present study—Figure 1). Kligfield et al. (1986) also reported ^{40}Ar-^{39}Ar furnace step-heating data on some of the same mineral separates, which gave internally discordant age spectra, with overall staircase shapes with increasing temperature, and high-temperature steps yielding ages up to ∼30–107 Ma but with total gas ages in line with the respective K-Ar ages. Kligfield et al. (1986) assigned the discordance to partial diffusive ^{40}Ar loss related to thermal disturbance at ∼14–12 Ma

and the anomalously old high-temperature steps to the contribution of inherited ^{40}Ar hosted in minor detrital white micas. The meaning of these step-heating experiments is, however, quite uncertain given the very fine grain sizes of the analyzed material (0.6–2 μm, 2–6 μm, and 6–20 μm) and the presence of chlorite in the mineral separates, which can cause analytical artifacts due to recoil loss/redistribution of Ar isotopes during sample irradiation (see e.g., Di Vincenzo et al., 2003). In light of the depositional age of the *Pseudomacigno* (the youngest stratigraphic unit involved in the Tertiary tectono-metamorphic events of the northern Apennines), which is believed to have occurred during the Rupelian (within ∼34–28 Ma) on the basis of temporal constraints brought by microfossils (zones P18–20 of planktonic foraminifera—Dallan-Nardi, 1977), Kligfield et al. (1986) concluded that the regional D1 foliation developed during a major folding event coeval with the regional greenschist facies metamorphism at ∼27 Ma. D2 structures formed instead locally at ∼12 Ma, when samples recorded a penetrative crenulation of the D1 foliation. Additionally, a non-oriented post-tectonic white mica developed later at ∼10–8 Ma. The meaningfulness of the older ages (Rupelian/Chattian boundary), assigned by Kligfield et al. (1986) to the onset of development of D1 structures, has recently been contended by Patacca et al. (2013) who inferred, on the basis of paleogeographic restorations and palinspastic reconstructions, that deformation and metamorphism in the Alpi Apuane cannot be older than the Aquitanian (∼23.0–20.4 Ma) and most likely as young as ∼12–11 Ma. Results from the present study define a temporal evolution for the D2 deformation in rough agreement with that proposed by Kligfield et al. (1986) but our data are only partially conclusive regarding the dispute over the onset of deformation. Although a dedicated ad hoc experimental study aimed at clarifying the onset of deformation in the northeastern Alpi Apuane and at verifying its possible diachronic evolution with respect to the southwestern sector is necessary, our data seem to favor a post-Chattian evolution but clearly exclude a post-Langhian age for the whole tectono-metamorphic evolution of the Apuane region.

5.2.2. Implications

Results from the present study provide first-order constraints useful to clarify some general issues still debated in the evolution of mountain belts (e.g., the rate of deformation, the duration of metamorphic events, and the superimposed and/or composite foliation development within polyphase or progressive deformation history) and, more specifically, address some open disputes concerning the regional geology of the northern Apennines. Within the limits set in a previous section (5.1. Interpretation of ^{40}Ar-^{39}Ar data and timing of deformation in the Alpi Apuane), key points arising from our investigation are summarized below, with their tectonic and regional implications.

1. The onset of metamorphism and deformation in the Alpi Apuane region has a minimum age of 20–21 Ma (Aquitanian/Burdigalian boundary), as documented by ^{40}Ar-^{39}Ar data for the composite D1 foliation and related structures in the western parts of the Alpi Apuane (i.e., Massa unit).
2. The D1 deformation, consistently with its composite character, occurred during a protracted metamorphic evolution, lasting at least ∼6.5 Ma from the Aquitanian/Burdigalian to the Langhian/Serravallian boundary (Figures 11a and 11b). A possible West-East diachronism for the development of D1 foliation cannot be excluded and it is suggested by the minimum age of ∼14.4 Ma obtained for the development of the D1 foliation in the easternmost sample of the Apuane Unit. Such a diachronism in the development of D1 foliation, although still to be verified, would be consistent with the West-East sense of transport, the stacking of the various units, and their internal deformation within the Alpi Apuane (Figures 10a and 10b), and it could therefore be significant from a tectonic viewpoint.
3. The D2 deformation shows a common temporal evolution at the scale of the entire Alpi Apuane region and is recorded for a duration of at least ∼2.5 Ma, starting not after the upper Serravallian and ending in the middle Tortonian, at ∼10.5 Ma, in the Massa Unit on the western side of the massif (Figure 11c).
4. The D2 deformation in the westernmost side of the Alpi Apuane (i.e., Massa Unit), was fluid assisted, with the introduction of Na-rich aqueous fluids, favoring the growth of paragonite, apparently absent during the D1 tectono-metamorphic event.

It is important to note that points (1), (2), and (3) weaken the arguments put forward by Patacca et al. (2013) against the interpretation of geochronological data proposed by Kligfield et al. (1986), specifically concerning their claim, based on paleogeographic reconstructions and geological restoration, of an age no older than 13–14 Ma for the tectono-metamorphic events in the Alpi Apuane. On the other hands, points (3) and (4) suggest that the D2 deformation structures, with kinematics features marking the switch from crustal contraction to crustal extension (Carmignani & Kligfield, 1990; Molli et al., 2018), have developed since the upper Serravallian, thus constraining

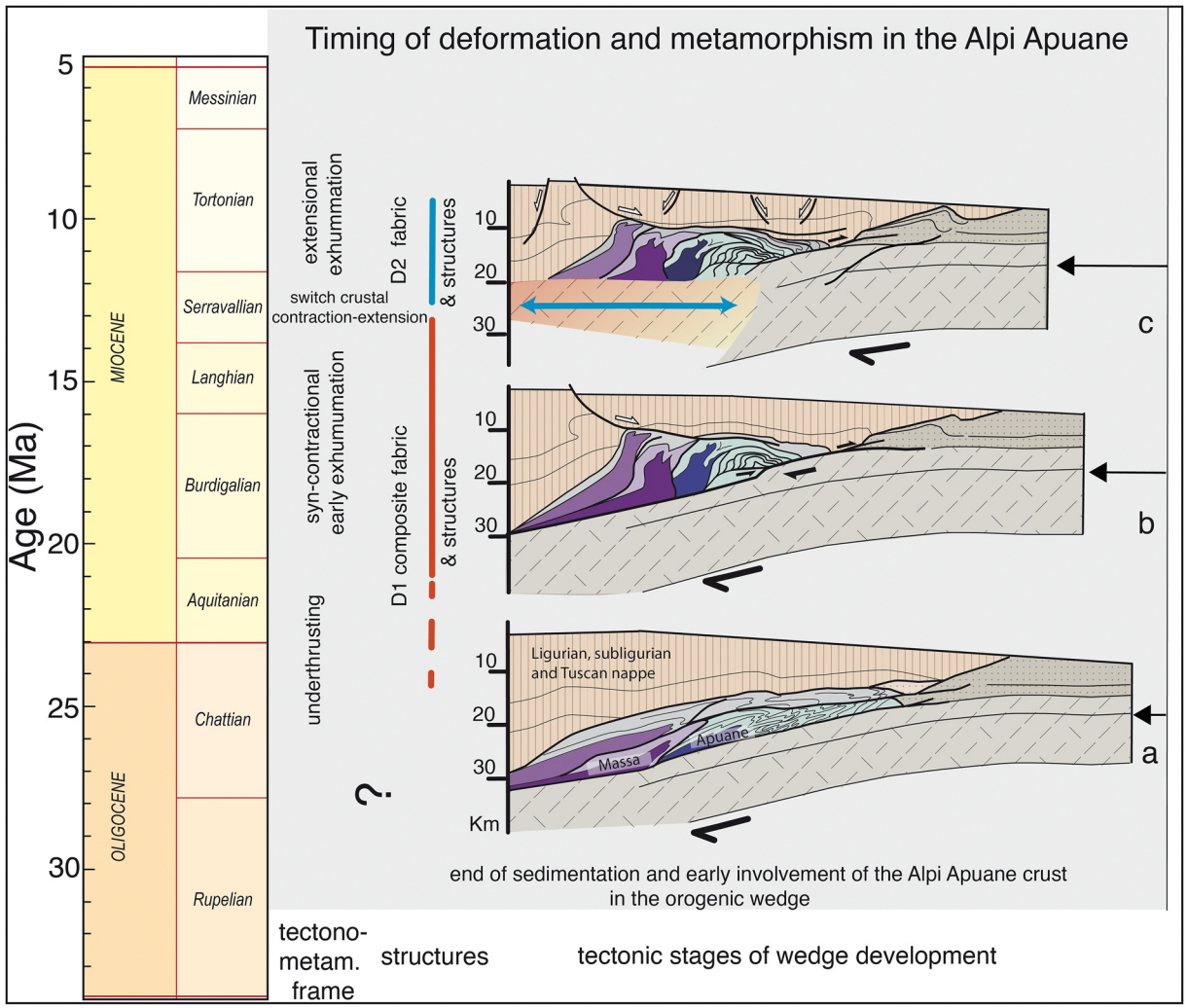

Figure 11. Evolutionary tectonic model and its temporal frame for the Alpi Apuane through the different kinematic stages of the Apenninic wedge growth (modified after Molli et al., 2018).

the onset of the genuine crustal extensional history in the inner northern Apennines at ~12.5–12.0 Ma. Moreover microchemical, geochronological, and micro- and meso-structural data linked to point (4) can indirectly be used to constrain the timing of the first coupling between the Massa Unit and the Tuscan nappe (Figures 2 and 11c), which in the former is marked by the appearance of paragonite. These units, initially separated by a minimum gap in pressure of ~0.2–0.3 GPa during the thickening stage (Molli et al., 2002, 2018), were then juxtaposed after an early stage of syn-contractional exhumation of the footwall metamorphic unit, associated with the thinning of the former nappe stack predating the development of D2 foliation in the Massa Unit (Figure 11c). It is important to note that the Tuscan Nappe includes in its basal part ancient levels of evaporites, now represented by the dolomite/carbonate-rich cataclasite of the *Calcare Cavernoso*, which acted as a major detachment surface (an early thrust later reactivated as a regional normal fault) and channeled a flow of Mg- and Na-rich fluids (Carter et al., 1994; Hodgkins & Stewart, 1994; Lugli et al., 2002), which could have provided the Na necessary for the stabilization of paragonite during the D2 crenulation in samples from the Massa Unit.

5.3. Implications for ^{40}Ar-^{39}Ar Dating of Low-Grade Deformation

Complications arising from the surviving of diachronous white-mica generations in low-to medium-grade metamorphic rocks have been previously tackled through different analytical strategies, involving: (a) in situ dating of rock chips (e.g., Cossette et al., 2015; Di Vincenzo et al., 2004; Schneider et al., 2013); (b) step-heating analyses

of white-mica separates (e.g., Villa et al., 2014); and (c) conventional K-Ar dating of different grain sizes of white mica (Akker et al., 2021; Berger et al., 2017). Dealing with low-to medium-grade metamorphic rocks, characterized by superimposed deformation events, together with the coexistence of diachronous white-mica generations at the submillimeter scale, in situ dating of rock chip seems in principle the best suited choice. However, several studies (e.g., Airaghi, Warren, et al., 2017; Beaudoin et al., 2020; Di Vincenzo et al., 2016; Villa & Hanchar, 2017) have shown that two main problems may potentially compromise the effectiveness of this technique: (a) the complex interplay between microstructures and microchemistry, which are not necessarily directly correlated and inevitably affect the Ar isotope record; (b) the intimate coexistence (down to the microscale) of diachronous white-mica generations, which would require in several cases a much higher spatial resolution than that achievable by the in situ laserprobe technique. A different way to disentangle coexisting diachronous and heterochemical white-mica generations exploits the step-heating extraction, which can potentially separate and analyze diachronous phases within single samples by differential breakdown reactions; diachronous phases can be qualitatively identified *a posteriori* using chemical information (K–Cl–Ca) from neutron-produced $^{39}Ar_K$, $^{37}Ar_{Ca}$, and $^{38}Ar_{Cl}$ in common-denominator three-isotope correlations plots (Villa & Hanchar, 2017) and whose resolution is limited by the recoil distances of argon isotopes during sample irradiation (with mean depletion depths by recoil in a semi-infinite medium of ∼80 nm for $^{39}Ar_K$ and ∼1 nm for $^{38}Ar_{Cl}$—Onstott et al., 1995). This analytical approach, combined with microtextural and microchemical data determined by the SEM and EMP, was successfully used for deconvolving diachronous white-mica generations through the Cl/K ratios (Villa et al., 2014). However, the strength of this approach relies on the recognition of true mineralogical end-member entities (in terms of Cl/K ratios), which need to be univocally identified in thin section. Implicit is that diachronous white-mica generations need to be characterized by significant chemical variations in order to produce distinct release patterns during in vacuo heating. A slightly different analytical strategy, which compares with the approach followed by O'Brien and van der Pluijm (2012) for deriving meaningful age from fault-generated pseudotachylyte, was recently presented by McAleer et al. (2021). They exploited a combination of modal estimates of two chemically distinct populations of coexisting muscovite from X-ray powder diffraction measurements and ^{40}Ar-^{39}Ar analyses. Data on different white-mica separates from a single hand specimen, characterized by different magnetic susceptibility, defined a mixing line that allowed to resolve the ages of both end members, relict versus newly formed white micas. However, such an approach is potentially effective only if the sample includes solely two white-mica generations, each developed within a restricted time interval (within the analytical uncertainty involved) and characterized by distinct chemical compositions. Other authors (e.g., Akker et al., 2021; Berger et al., 2017) exploited a grain-size sensitive analytical approach, similar to that used to investigate fault gouges (Zwingman et al., 2004), together with X-ray powder diffraction measurements, and microstructural and microchemical analysis. The K-Ar method was preferred over the variant ^{40}Ar-^{39}Ar, to overcome analytical artifacts in very fine grain sizes due to $^{39}Ar_K$ recoil during sample irradiation. Akker et al. (2021), investigating resetting processes of detrital white mica in samples from a prograde sedimentary sequence (from ∼200 to 330°C), found that increasing recrystallization by dissolution-reprecipitation processes was the main factor inducing chemical reset of the detrital isotopic record, but white-mica chemistry revealed no simple relationship between isotopic reset and grain size along the prograde path. Geologically meaningful dates were obtained only for the smaller grain sizes in the most deformed rocks under the highest metamorphic grade.

Based on the arguments presented above, none of the analytical approaches mentioned should be considered ideal and effective for any experimental study aimed at reconstructing deformation histories, and the best analytical strategy should be evaluated on a case-by-case basis. In this study, similar to other works (e.g., Beaudoin et al., 2020; Cardello et al., 2019; Di Vincenzo et al., 2016; Kellett et al., 2016), we combined the results of both in situ and step-heating techniques, complemented by structural and chemical investigation at the microscale. Cl contents of white mica determined by the electron microprobe were generally close or below the detection limit (Table S1), in agreement with low $^{38}Ar_{Cl}$ intensities in both step-heating and in situ data (Cl/K ratios from neutron-produced $^{39}Ar_K$ and $^{38}Ar_{Cl}$, <<0.001), and this made three-isotope correlation diagrams (based on $^{40}Ar^*$, $^{39}Ar_K$, and $^{38}Ar_{Cl}$ isotopes) useless. It is important to note that when comparing in situ and step-heating data, results are not necessarily directly comparable. Indeed, in the present study the volume investigated by the Ar laserprobe for a single in situ analysis (∼10^{-3} mm^3) is nearly 1,500 times smaller than that of the mineral separates that were analyzed by the step-heating technique. Likewise, the areas investigated by the Ar laserprobe (10^4 μm^2) are significantly larger than those analyzed by the electron microprobe (∼10 μm^2). If on the one hand ^{40}Ar-^{39}Ar data from the two extraction techniques yield similar total gas ages, on the other hand the

distribution of Ar ages is mostly different, and most of the concordant segments defined by step-heating data have no correspondence in the distribution of in situ data and, with the only exception of sample 22, they are geologically meaningless. More specifically, in samples 22 and 265 of the Massa Unit, step-heating data tend to average the isotopic compositions of white mica and reflect the bulk composition of the whole hand specimen, losing important information on the evolution of the D2 crenulation. In the most retrogressed sample 22, step-heating data yielded ages compatible with the in situ data performed in the quartz-calcite matrix but bear no evident record of the concordant ages detected by in situ dating of the pelitic layers. The age spectrum of sample 265 is instead likely plagued by an extraneous component, attributable to the isotope record of white mica from the chloritoid-bearing domains identified by in situ analysis, and whose Ar ages are of uncertain meaning. Step-heating data on white-mica separates of samples from the Apuane Unit gave slightly discordant age spectra, with concordant segments representing more than 60% of the $^{39}Ar_K$ released. In contrast in situ data from both samples gave a nearly continuous variation, with a significant age interval of more than 3 Ma. A simple explanation for this contrasting behavior can be found in the weak chemical variation of white mica from the Apuane Unit, which may have prompted the step-heating technique to homogenize the small-scale isotope heterogeneity that was, however, revealed by the ^{40}Ar-^{39}Ar spatially controlled analysis (cf. Kellet et al., 2016). The above arguments therefore suggest that because of the lithological heterogeneity at the scale of the hand specimen and of compositionally driven strain partitioning, together with the volumetrically different scale of the sample investigated by the two extraction techniques, the in situ ^{40}Ar-^{39}Ar laser analysis gave more reliable and complete results. Indeed, it is important to note that the presence of intrasample discordant ages implies that the isotope disequilibrium, due to the presence of diachronous white-mica generation, was not entirely homogenized and blurred by the Ar laserprobe, otherwise in situ data would have tended to intrasample concordant apparent ages.

From a broad perspective, the results from the present work reiterate the intrinsic difficulties involved in ^{40}Ar-^{39}Ar dating of deformation in low- to medium-grade metamorphic rocks and highlight the great importance of a detailed microscale characterization and of a careful preselection of samples, as compositionally different domains only a few millimeters apart within the same specimen may yield significantly different results because of compositionally driven strain partitioning. It is, however, evident, in agreement with previous studies (e.g., Akker et al., 2021), that for partially retrogressed early fabrics, white mica only records minimum ages of the older deformation, whereas the youngest age limit approaches the geologically meaningful age of the younger event as retrogression becomes more pervasive. The pattern defined by the development of paragonite during the D2 crenulation in samples from the Massa Unit demonstrates, as already noted in other studies (e.g., Airaghi, Lanari, et al., 2017; Beaudoin et al., 2020), that chemical reequilibration followed a complex interplay among deformation mechanism, finite strain, and dissolution-reprecipitation processes. Specifically, microstructural and microchemical data reveal that although paragonite preferentially developed in the most pelitic domains, where the D2 crenulation schistosity is more pervasive, it is also well-developed along the older D1 schistosity, indicating that chemical reequilibration occurred along a front, likely proceeding from the D2 schistosity, rather than simply following the finite strain record. Even though the complex interplay among deformation mechanism, finite strain, and dissolution-reprecipitation processes mentioned above may explain why each schistosity in samples from Apuane Unit yielded internally discordant rather than discrete ages, it remains uncertain whether the dispersion within the samples investigated is at least partially due to dynamic closure, which occurred during a protracted deformation event.

Data Availability Statement

Data sets, including EMP data (Table S1) and ^{40}Ar-^{39}Ar data (Table S2), are available in the Mendeley Data repository, at https://data.mendeley.com/datasets/b9d7kzfvcd/draft?a=30540da4-256e-4251-834f-35ecc4612811.

Acknowledgments
Constructive comments and suggestions by R. Augier and by an anonymous reviewer and the editorial handling by L. Jolivet and the associated editor D. Grujic are very much appreciated. Research was financially supported by Consiglio Nazionale delle Ricerche (CNR) and Pisa University Ateneo Funds. The Ar laserprobe facility was realized with the financial support of CNR. Open Access Funding provided by Consiglio Nazionale delle Ricerche within the CRUI-CARE Agreement.

References

Abbate, E., Balestrieri, M. L., Bigazzi, G., Norelli, P., & Quercioli, C. (1994). Fission-track datings and recent rapid denudation in northern Apennines, Italy. *Memorie della Società Geologica Italiana*, *48*, 579–585.

Airaghi, L., Lanari, P., de Sigoyer, J., & Guillot, S. (2017). Microstructural vs compositional preservation and pseudomorphic replacement of muscovite in deformed metapelites from the Longmen Shan (Sichuan, China). *Lithos*, *282–283*, 262–280. https://doi.org/10.1016/j.lithos.2017.03.013

Airaghi, L., Warren, C. J., de Sigoyer, J., Lanari, P., & Magnin, V. (2017). Influence of dissolution/reprecipitation reactions on metamorphic greenschist to amphibolite-facies mica $^{40}Ar/^{39}Ar$ ages in the Longmen Shan (Eastern Tibet). *Journal of Metamorphic Geology*, *36*(7), 933–958. https://doi.org/10.1111/jmg.12420

Akker, I. V., Berger, A., Zwingmann, H., Todd, A., Schrank, C. E., Jones, M. W. M., et al. (2021). Structural and chemical resetting processes in white mica and their effect on K-Ar data during low temperature metamorphism. *Tectonophysics*, *800*, 228708. https://doi.org/10.1016/j.tecto.2020.228708

Augier, R., Agard, P., Monié, P., Jolivet, L., Robin, C., & Booth-Rea, G. (2005). Exhumation, doming and slab retreat in the Betic Cordillera (SE Spain): In situ $^{40}Ar/^{39}Ar$ ages and P–T–d–t paths for the Nevado-Filabride complex. *Journal of Metamorphic Geology*, *23*(5), 357–381. https://doi.org/10.1111/j.1525-1314.2005.00581.x

Beaudoin, A., Scaillet, S., Mora, N., Jolivet, L., & Augier, R. (2020). In situ and step-heating 40Ar/39Ar dating of white mica in low-temperature shear zones (Tenda massif, Alpine Corsica, France). *Tectonics*, *39*(12), e2020TC006246. https://doi.org/10.1029/2020TC006246

Berger, A., Wehrens, P., Lanari, P., Zwingmann, H., & Herwegh, M. (2017). Microstructures, mineral chemistry and geochronology of white micas along a retrograde evolution: An example from the Aar massif (Central Alps, Switzerland). *Tectonophysics*, *721*, 179–195. https://doi.org/10.1016/j.tecto.2017.09.019

Cardello, G. L., Di Vincenzo, G., Giorgetti, G., Zwingmann, H., & Mancktelow, N. (2019). Initiation and development of the Pennine basal thrust (Swiss Alps): A structural and geochronological study of an exhumed megathrust. *Journal of Structural Geology*, *126*, 338–356. https://doi.org/10.1016/j.jsg.2019.06.014

Carmignani, L., Giglia, G., & Kligfield, R. (1978). Structural evolution of the Apuane Alps: An example of continental margin deformation in the Northern Apennine. *Journal of Geology*, *86*(4), 487–504. https://doi.org/10.1086/649714

Carmignani, L., & Kligfield, R. (1990). Crustal extension in the northern Apennines: The transition from compression to extension in the Alpi Apuane core complex. *Tectonics*, *9*(6), 1275–1303. https://doi.org/10.1029/TC009i006p01275

Carosi, R., Leoni, L., Montomoli, C., & Sartori, F. (2003). Very low-grade metamorphism in the Tuscan Nappe, northern Apennines, Italy: Relationships between deformation and metamorphic indicators in the La Spezia mega-fold. *Schweizerische Mineralogische und Petrographische Mitteilungen*, *83*, 15–32.

Carter, K. E., Dworkin, S. I., Carmignani, L., Meccheri, M., & Fantozzi, P. (1994). Dating thrust events using $^{87}Sr/^{86}Sr$: An example from the northern Apennines. *The Journal of Geology*, *10*(3), 297–305. https://doi.org/10.1086/629672

Cerrina Feroni, A. G., Plesi, G., Fanelli, G., Leoni, L., & Martinelli, P. (1983). Contributo alla conoscenza dei processi metamorfici di grado molto basso (anchi-metamorfismo) a carico della falda toscana nell'area del ricoprimento apuano. *Bolletino Società Geologica Italiana*, *102*, 269–280.

Ciarapica, G., & Passeri, L. (2002). The palaeogeographic duplicity of the Apennines. *Bollettino Società Geologica Italiana*, *1*, 67–75.

Conti, P., Carmignani, L., Massa, G., Meccheri, M., Patacca, E., Scandone, P., & Pieruccioni, D. (2020). *Note illustrative CARG Foglio 249 Massa* (p. 290). ISPRA.

Conti, P., Gattiglio, M., & Meccheri, M. (1991). The overprint of the Alpine tectonometamorphic evolution on the Hercynian orogen: An example from the Apuane Alps (northern Apennines, Italy). *Tectonophysics*, *191*(3–4), 335–346. https://doi.org/10.1016/0040-1951(91)90066-2

Cossette, É., Schneider, D. A., Warren, C. J., & Grasemann, B. (2015). Lithological, rheological, and fluid infiltration control on $^{40}Ar/^{39}Ar$ ages in polydeformed rocks from the West Cycladic detachment system, Greece. *Lithosphere*, *7*(2), 189–205. https://doi.org/10.1130/L416.1

Costa, E., Pialli, G., & Plesi, G. (1998). Foreland basins of the northern Apennines: Relationships with passive subduction of the Adriatic lithosphere. *Memorie della Società Geologica Italiana*, *52*, 595–606.

Dallan-Nardi, L. (1977). Segnalazione di Lepidocycline nelle parte basale dello "pseudomacigno" delle Alpi Apuane. *Bollettino della Società Geologica Italiana*, *95*, 459–477.

Dempster, T. J. (1992). Zoning and recrystallization of phengitic micas: Implications for metamorphic equilibration. *Contributions to Mineralogy and Petrology*, *109*(4), 526–537. https://doi.org/10.1007/BF00306554

Di Vincenzo, G., Carosi, R., & Palmeri, R. (2004). The relationship between tectono–metamorphic evolution and argon isotope records in white mica: Constraints from in situ ^{40}Ar–^{39}Ar laser analysis of the variscan basement of Sardinia (Italy). *Journal of Petrology*, *45*(5), 1013–1043. https://doi.org/10.1093/petrology/egh002

Di Vincenzo, G., Folco, L., Suttle, M. D., Brase, L., & Harvey, R. P. (2021). Multi-collector $^{40}Ar/^{39}Ar$ dating of microtektites from Transantarctic mountains (Antarctica): A definitive link with the Australasian tektite/microtektite strewn field. *Geochimica et Cosmochimica Acta*, *298*, 112–130. https://doi.org/10.1016/j.gca.2021.01.046

Di Vincenzo, G., Grande, A., Prosser, G., Cavazza, W., & DeCelles, P. G. (2016). ^{40}Ar–^{39}Ar laser dating of ductile shear zones from central Corsica (France): Evidence of Alpine (middle to late Eocene) syn-burial shearing in Variscan granitoids. *Lithos*, *262*, 369–383. https://doi.org/10.1016/j.lithos.2016.07.022

Di Vincenzo, G., & Skála, R. (2009). ^{40}Ar–^{39}Ar laser dating of tektites from the Cheb basin (Czech Republic): Evidence for coevality with moldavites and influence of the dating standard on the age of the Ries impact. *Geochimica et Cosmochimica Acta*, *73*(2), 493–513. https://doi.org/10.1016/j.gca.2008.10.002

Di Vincenzo, G., Viti, C., & Rocchi, R. (2003). The effect of chlorite interlayering on ^{40}Ar–^{39}Ar biotite dating: An ^{40}Ar–^{39}Ar laserprobe and TEM investigation of variably chloritised biotites. *Contributions to Mineralogy and Petrology*, *145*(6), 643–658. https://doi.org/10.1007/s00410-003-0472-z

Fellin, M. G., Reiners, P. W., Brandon, M. T., Wuthrich, E., Balestrieri, M. L., & Molli, G. (2007). Thermochronologic evidence for exhumational history of the Alpi Apuane metamorphic core complex, northern Apennines, Italy. *Tectonics*, *26*(6), TC6015. https://doi.org/10.1029/2006TC002085

Franceschelli, M., Leoni, L., Memmi, I., & Puxeddu, M. (1986). Regional distribution of Al-silicates and metamorphic zonation in the low-grade Verrucano metasediments from the northern Apennines, Italy. *Journal Metamorphic Geology*, *4*(3), 309–321. https://doi.org/10.1111/j.1525-1314.1986.tb00353.x

Franceschelli, M., & Memmi, I. (1999). Zoning of chloritoid from kyanite-facies metapsammites, Alpi Apuane, Italy. *Mineralogical Magazine*, *63*(1), 105–110. https://doi.org/10.1180/minmag.1999.063.1.10

Franceschelli, M., Memmi, I., Carangiu, G., & Gianelli, G. (1997). Prograde and retrograde chloritoid zoning in low temperature metamorphism, Alpi Apuane, Italy. *Schweizerische Mineralogische und Petrographische Mitteilungen*, *77*, 41–50.

Giglia, G., & Radicati di Brozolo, F. (1970). K/Ar age of metamorphism in the Apuane Alps (Northern Tuscany). *Bollettino della Società Geologica Italiana*, *89*, 485–497.

Guidotti, C. V. (1984). Micas in metamorphic rocks. In S. W. Bailey (Ed.), *Micas. Reviews in mineralogy* (Vol. 13, pp. 257–468). Mineralogical Society of America.

Guidotti, C. V., Sassi, F. P., Blencoe, J. G., & Selverstone, J. (1994). The paragonite-muscovite solvus: I. P-T-X limits derived from the Na-K compositions of natural, quasibinary paragonite-muscovite pairs. *Geochimica et Cosmochimica Acta*, *58*(10), 2269–2275. https://doi.org/10.1016/0016-7037(94)90009-4

Harrison, T. M., Célérier, J., Aikman, A. B., Hermann, J., & Heizler, M. T. (2009). Diffusion of ^{40}Ar in muscovite. *Geochimica et Cosmochimica Acta*, *73*(4), 1039–1051. https://doi.org/10.1016/j.gca.2008.09.038

Hodgkins, M. A., & Stewart, K. G. (1994). The use of fluid inclusions to constrain fault zone pressure temperature and kinematic history: An example from the Alpi Apuane, Italy. *Journal of Structural Geology*, *16*(1), 85–96. https://doi.org/10.1016/0191-8141(94)90020-5

Holland, T. J. B., & Powell, R. (2011). An improved and extended internally consistent thermodynamic dataset for phases of petrological interest, involving a new equation of state for solids. *Journal of Metamorphic Geology*, *29*(3), 333–383. https://doi.org/10.1111/j.1525-1314.2010.00923.x

Jicha, B. R., Singer, B. S., & Sobol, P. (2016). Re-evaluation of the ages of ^{40}Ar/^{39}Ar sanidine standards and supereruptions in the Western U.S. using a Noblesse multi-collector mass spectrometer. *Chemical Geology*, *431*, 54–66. https://doi.org/10.1016/j.chemgeo.2016.03.024

Jolivet, L., Faccenna, C., Goffé, B., Mattei, M., Rossetti, F., Brunet, C., et al. (1998). Midcrustal shear zones in postorogenic extension: Example from the Northern Tyrrhenian Sea. *Journal of Geophysical Research, Solid Earth*, *103*(B6), 12123–12160. https://doi.org/10.1029/97JB03616

Kellett, D. A., Warren, C., Larson, K. P., Zwingmann, H., van Staal, C. R., & Rogers, N. (2016). Influence of deformation and fluids on Ar retention in white mica: Dating the Dover Fault, Newfoundland Appalachians. *Lithos*, *254–255*, 1–17. https://doi.org/10.1016/j.lithos.2016.03.003

Kligfield, R., Hunziker, J., Dallmeyer, R. D., & Schamel, S. (1986). Dating of deformation phases using K-Ar and ^{40}Ar/^{39}Ar techniques: Results from the northern Apennines. *Journal of Structural Geology*, *8*(7), 781–798. https://doi.org/10.1016/0191-8141(86)90025-8

Kuiper, K. F., Deino, A., Hilgen, F. J., Krijgsman, W., Renne, P. R., & Wijbrans, J. R. (2008). Synchronizing rock clocks of Earth history. *Science*, *320*(5875), 500–504. https://doi.org/10.1126/science.1154339

Le Breton, E., Handy, M., Molli, G., & Ustaszewski, K. (2017). Post-20 Ma motion of the Adriatic plate – New constraints from surrounding orogens and implications for crust-mantle decoupling. *Tectonics*, *36*(12), 3135–3154. https://doi.org/10.1002/2016TC004443

Lee, J.-Y., Marti, K., Severinghaus, J. P., Kawamura, K., Yoo, H.-S., Lee, J. B., & Kim, J. S. (2006). A redetermination of the isotopic abundances of atmospheric Ar. *Geochimica et Cosmochimica Acta*, *70*(17), 4507–4512. https://doi.org/10.1016/j.gca.2006.06.1563

Ludwig, K. R. (2012). *Isoplot/Ex version 3.75, A geochronological toolkit for microsoft excel*. Berkeley Geochronology Center Special Publications, No. 5.

Lugli, S., Morteani, G., & Blamart, D. (2002). Petrographic, REE, fluid inclusion and stable isotope study of magnesite from the Upper Triassic Burano evaporites (Secchia valley, northern Apennines): Contribution from sedimentary, hydrothermal and metasomatic sources. *Mineralium Deposita*, *37*(5), 480–494. https://doi.org/10.1007/s00126-001-0251-6

Mark, D. F., Barfod, D., Stuart, F. M., & Imlach, J. (2009). The ARGUS multicollector noble gas mass spectrometer: Performance for ^{40}Ar/^{39}Ar geochronology. *Geochemistry, Geophysics, Geosystems*, *10*(2), 1–9. https://doi.org/10.1029/2009GC002643

Martini, I. P., Rau, A., & Tongiorgi, M. (1986). Syntectonic sedimentation in a Middle Triassic rift, Northern Apennines, Italy. *Sedimentary Geology*, *47*(3–4), 191–219. https://doi.org/10.1016/0037-0738(86)90084-9

McAleer, R. J., Bish, D. L., Kunk, M. J., Valley, P. M., Walsh, G. J., & Wintsch, R. P. (2021). Unmixing multiple metamorphic muscovite age populations with powder x-ray diffraction and ^{40}Ar/^{39}Ar analysis. *American Journal of Science*, *321*(3), 332–364. https://doi.org/10.2475/03.2021.02

McDougall, I., & Harrison, T. M. (1999). *Geochronology and thermochronology by the ^{40}Ar/^{39}Ar method* (p. 269). Oxford University Press.

Min, K., Mundil, R., Renne, P. R., & Ludwig, K. R. (2000). A test for systematic errors in ^{40}Ar/^{39}Ar geochronology through comparison with U/Pb analysis of a 1.1-Ga rhyolite. *Geochimica et Cosmochimica Acta*, *64*(1), 73–98. https://doi.org/10.1016/S0016-7037(99)00204-5

Mixon, E. E., Jicha, B. R., Tootell, D., & Singer, B. S. (2022). Optimizing ^{40}Ar/^{39}Ar analyses using an Isotopx NGX-600 mass spectrometer. *Chemical Geology*, *593*, 120753. https://doi.org/10.1016/j.chemgeo.2022.120753

Molli, G. (2008). Northern Apennine-Corsica orogenic system: An updated review. In S. Siegesmund, B. Fügenschuh, & N. Froitzheim (Eds.), *Tectonic aspects of the alpine-dinaride-carpathian system* (Vol. 298, pp. 413–442). Geological Society of London Special Publication.

Molli, G., Brogi, A., Caggianelli, A., Capezzuoli, E., Liotta, D., Spina, A., & Zibra, I. (2020). Late Palaeozoic tectonics in Central Mediterranean: A reappraisal. *Swiss Journal of Geosciences*, *113*(1), 23. https://doi.org/10.1186/s00015-020-00375-1

Molli, G., Conti, P., Giorgetti, G., Meccheri, M., & Oesterling, N. (2000). Microfabric studies on the deformation and thermal history of the Alpi Apuane marbles (Carrara marbles), Italy. *Journal of Structural Geology*, *22*(11–12), 1809–1825. https://doi.org/10.1016/S0191-8141(00)00086-9

Molli, G., Giorgetti, G., & Meccheri, M. (2000). Structural and petrological constraints on the tectonometamorphic evolution of the Massa unit (Alpi Apuane, NW Tuscany, Italy). *Geological Journal*, *35*(3–4), 251–264. https://doi.org/10.1002/gj.860

Molli, G., Giorgetti, G., & Meccheri, M. (2002). Tectono-metamorphic evolution of the Alpi Apuane metamorphic complex: New data and constraints for geodynamic models. *Bollettino della Società Geologica Italiana*, *1*, 789–800.

Molli, G., Manighetti, I., Bennett, R., Malavieille, J., Serpelloni, E., Storti, F., et al. (2021). Active fault systems in the inner northwest Apennines, Italy: A reappraisal one century after the 1920 Mw ∼6.5 Fivizzano earthquake. *Geosciences*, *11*(3), 139. https://doi.org/10.3390/geosciences11030139

Molli, G., & Meccheri, M. (2012). Structural inheritance and style of reactivation at mid-crustal levels: A case study from the Alpi Apuane (Tuscany, Italy). *Tectonophysics*, *579*, 74–87. https://doi.org/10.1016/j.tecto.2012.06.044

Molli, G., Vitale Brovarone, A., Beyssac, O., & Cinquini, I. (2018). RSCM thermometry in the Alpi Apuane (NW Tuscany, Italy): New constraints for the metamorphic and tectonic history of the inner northern Apennines. *Journal of Structural Geology*, *113*, 200–216. https://doi.org/10.1016/j.jsg.2018.05.020

Molli, G., White, J. C., Kennedy, L., & Taini, V. (2011). Low-temperature deformation of limestone, Isola Palmaria, Northern Apennine, Italy—The role of primary textures, precursory veins and intracrystalline deformation in localization. *Journal of Structural Geology*, *33*(3), 255–270. https://doi.org/10.1016/j.jsg.2010.11.015

Mulch, A., Cosca, M., & Handy, M. (2002). In-situ UV-laser ^{40}Ar/^{39}Ar geochronology of a micaceous mylonite: An example of defect-enhanced argon loss. *Contributions to Mineralogy and Petrology*, *142*(6), 738–752. https://doi.org/10.1007/s00410-001-0325-6

Niespolo, E. M., Rutte, D., Deino, A. L., & Renne, P. R. (2017). Intercalibration and age of the Alder Creek sanidine ^{40}Ar/^{39}Ar standard. *Quaternary Geochronology*, *39*, 205–213. https://doi.org/10.1016/j.quageo.2016.09.004

Nteme, J., Scaillet, S., Brault, P., & Tassan-Got, L. (2022). Atomistic simulations of ^{40}Ar diffusion in muscovite. *Geochimica et Cosmochimica Acta*. in press. https://doi.org/10.1016/j.gca.2022.05.004

O'Brien, T. M., & van der Pluijm, B. A. (2012). Timing of Iapetus Ocean rifting from Ar geochronology of pseudotachylytes in the St. Lawrence rift system of Southern Quebec. *Geology*, *40*(5), 443–446. https://doi.org/10.1130/G32691.1

Onstott, T. C., Miller, M. L., Ewing, R. C., Arnold, G. W., & Walsh, D. S. (1995). Recoil refinements: Implications for the ^{40}Ar/^{39}Ar dating technique. *Geochimica et Cosmochimica Acta*, *59*(9), 1821–1834. https://doi.org/10.1016/0016-7037(95)00085-E

Patacca, E., Scandone, P., Conti, P., Mancini, S., & Massa, G. (2013). Ligurian-derived olistostrome in the pseudomacigno formation of the Stazzema zone (Alpi Apuane, Italy). Geological implications at regional scale. *Italian Journal of Geosciences*, *132*(3), 463–476. https://doi.org/10.3301/IJG.2013.05

Patacca, E., Scandone, P., Meccheri, M., & Massa, G. (2011). Stratigraphic and structural revision of the Massa "Schuppenzone" (Alpi Apuane, northern Apennines). *Rendiconti online Società Geologica Italiana*, *15*, 102–105.

Phillips, D., & Matchan, E. L. (2013). Ultra-high precision $^{40}Ar/^{39}Ar$ ages for fish canyon tuff and Alder Creek Rhyolite sanidine: New dating standards required? *Geochimica et Cosmochimica Acta*, *121*, 229–239. https://doi.org/10.1016/j.gca.2013.07.003

Schneider, S., Hammerschmidt, K., & Rosenberg, C. L. (2013). Dating the longevity of ductile shear zones: Insight from $^{40}Ar/^{39}Ar$ in situ analyses. *Earth and Planetary Science Letters*, *369–370*, 43–58. https://doi.org/10.1016/j.epsl.2013.03.002

Storti, F. (1995). Tectonics of the Punta Bianca promontory: Insights for the evolution of the Northern Apennines-Northern Tyrrhenian Sea basin. *Tectonics*, *14*(4), 832–847. https://doi.org/10.1029/95TC01203

Vezzoni, S., Biagioni, C., D'Orazio, M., Pieruccioni, D., Galanti, Y., Petrelli, M., & Molli, G. (2018). Evidence of Permian magmatism in the Alpi Apuane metamorphic complex (northern Apennines, Italy): New hints for the geological evolution of the basement of the Adria plate. *Lithos*, *318–319*, 104–123. https://doi.org/10.1016/j.lithos.2018.08.003

Villa, I. M. (2021). The in vacuo release of Ar from minerals: 1. Hydrous minerals. *Chemical Geology*, *564*, 120076. https://doi.org/10.1016/j.chemgeo.2021.120076

Villa, I. M., Bucher, S., Bousquet, R., Kleinhanns, I. C., & Schmid, S. M. (2014). Dating polygenetic metamorphic assemblages along a transect through the Western Alps. *Journal of Petrology*, *55*(4), 803–830. https://doi.org/10.1093/petrology/egu007

Villa, I. M., & Hanchar, J. M. (2017). Age discordance and mineralogy. *American Mineralogist*, *102*(12), 2422–2439. https://doi.org/10.2138/am-2017-6084

Villa, I. M., & Puxeddu, M. (1994). Geochronology of the Larderello geothermal field: New data and the "closure temperature" issue. *Contributions to Mineralogy and Petrology*, *115*(4), 415–426. https://doi.org/10.1007/BF00320975

Whitney, D. L., & Evans, B. W. (2010). Abbreviations for names of rock-forming minerals. *American Mineralogist*, *95*(1), 185–187. https://doi.org/10.2138/am.2010.3371

Zwingmann, H., Offler, R., Wilson, T., & Cox, S. (2004). K–Ar dating of fault gouge in the northern Sydney basin, NSW, Australia—Implications for the breakup of Gondwana. *Journal of Structural Geology*, *26*(12), 2285–2295. https://doi.org/10.1016/j.jsg.2004.03.007